

Interseismic Strain Accumulation Across the Main Recent Fault, SW Iran, From Sentinel-1 InSAR Observations

Andrew R. Watson¹ , John R. Elliott¹ , and Richard J. Walters² 

¹COMET, School of Earth and Environment, University of Leeds, Leeds, UK, ²Department of Earth Sciences, COMET, Durham University, Durham, UK

Key Points:

- We derive East and Vertical surface velocities from 5.5 years of Sentinel-1 synthetic aperture radar images over the western Zagros
- We estimate an interseismic slip rate of 2.4 ± 1.2 mm/yr (2σ) for the Main Recent Fault, in agreement with previous GNSS studies
- We estimate a geodetically-determined interseismic locking depth of 14 km with a large uncertainty of 6–40 km, a first for this fault

Supporting Information:

Supporting Information may be found in the online version of this article.

Correspondence to:

A. R. Watson,
eearw@leeds.ac.uk

Citation:

Watson, A. R., Elliott, J. R., & Walters, R. J. (2022). Interseismic strain accumulation across the Main Recent Fault, SW Iran, from Sentinel-1 InSAR observations. *Journal of Geophysical Research: Solid Earth*, 127, e2021JB022674. <https://doi.org/10.1029/2021JB022674>

Received 2 JUL 2021
Accepted 28 JAN 2022

© 2022. The Authors.
This is an open access article under the terms of the [Creative Commons Attribution License](https://creativecommons.org/licenses/by/4.0/), which permits use, distribution and reproduction in any medium, provided the original work is properly cited.

Abstract The Main Recent Fault is a major right-lateral strike-slip fault in the western Zagros mountains of Iran. Recent geodetic and geological studies estimate a low slip rate of 1–6 mm/yr at an unknown depth which, when combined with a non-ideal fault geometry, makes the Main Recent Fault a difficult but interesting target for InSAR analysis. This analysis would further cement the estimated slip rate and provide an opportunity of estimate the depth to the base of the locked seismogenic zone, both important constraints on the seismic hazard posed by the fault, as well as for understanding how oblique convergence is accommodated and partitioned across the Zagros. We use 200 Sentinel-1 SAR images from the past 5 years, spanning two ascending and two descending tracks, to estimate the first InSAR-derived slip rate and locking depth for a 300 km long section of the fault. We utilize two established processing systems, LICsAR and LICsBAS, to produce interferograms and perform time series analysis, respectively. We constrain north-south motion using GNSS observations, decompose our InSAR line-of-sight velocities into fault-parallel and vertical motion, and fit 1-D screw dislocation models to three fault-perpendicular profiles of fault-parallel velocity, following a Bayesian approach to estimate the posterior probability distribution on the fault parameters. We estimate an interseismic slip velocity of 2.4 ± 1.2 mm/yr below a loosely constrained 14 km locking depth, the first such estimate for the fault, and discuss the challenges in constraining the locking depth for low magnitude interseismic signals.

Plain Language Summary Convergence between the Arabian and Eurasian plates is causing deformation of the Earth's crust in Iran. Some of this motion is taken up by movement at depth on the Main Recent Fault, which is stuck by friction near the Earth's surface and is therefore accumulating strain which may then be released in an earthquake. We use 5 years of satellite radar images to measure the average velocity of the ground surface either side of the fault. By looking at the velocity difference across the fault, along with the gradient, we can estimate the rate at which the fault is accumulating strain and the depth below which this is occurring. Our estimated rate of 2.4 ± 1.2 mm/yr is in agreement with previous estimates from GPS studies, while our locking depth estimate of 14 km with a large uncertainty of 6–40 km, is the first such estimate for the fault. The broad range of possible values for the locking depth highlights the difficulties of studying tectonic signals when they are close in magnitude to the sensing limit of our satellite imagery method (1 mm/yr).

1. Introduction

The Main Recent Fault (MRF) is a 800 km long dextral strike-slip fault in the hinterlands of the Zagros mountains, Iran. The fault is one of the most seismically active in the northwestern Zagros, having experienced historical earthquakes up to M_s 7.4 (Ambraseys & Moinfar, 1973; Ghods et al., 2012; Karasözen et al., 2019), driven by convergence between the Arabian and Eurasian plates. During the interseismic period of the earthquake cycle, the MRF can be viewed as accumulating strain in the locked upper crust whilst slipping aseismically at depth, following that assumed for other strike-slip fault zones (Savage, 2000; Savage & Prescott, 1978; Thatcher, 1983; Wright et al., 2013). Estimates of interseismic slip rate and the depth-extent of the locked seismogenic zone, from here on referred to as the “locking depth”, are critical to our understanding of both the local seismic hazard (Smith-Konter & Sandwell, 2009), and the accommodation of oblique convergence across the Zagros. Previous studies of the MRF have used a range of geological markers, geomorphological offsets, cosmogenic isotope dating, and Global Navigation Satellite System (GNSS) measurements to estimate a wide range (1–17 mm/yr) of possible slip rates (Table 1). The average slip rates determined from long-term geological/geomorphological offsets (1.6–17 mm/yr; Alipoor et al., 2012; Bachmanov et al., 2004; Copley & Jackson, 2006; Talebian & Jackson, 2002) and cosmogenic dating (3.5–12.5 mm/yr, Authemayou et al., 2009) cover a broader range with higher upper bounds than geodetic slip rates from decadal GNSS studies (1–7 mm/yr; Hessami et al., 2006; Khorrami

Table 1

Previously Published Long-Term Geologic and Geodetic Interseismic Slip Rate Estimates for the Main Recent Fault (Top) and Adjacent Faults (Bottom)

Study	Fault	Method	Rate (mm/yr)
Talebian and Jackson (2002)	MRF	Geological/geomorphological features	10–17
Bachmanov et al. (2004)	MRF: Dorud & Nahavand segments	Geological/geomorphological features	10
Vernant et al. (2004)	MRF	GNSS (regional)	3 ± 2
Copley and Jackson (2006)	MRF	Geological/geomorphological features	2–5
Walpersdorf et al. (2006)	MRF	GNSS (regional)	4–6
Authemayou et al. (2009)	MRF	Cosmogenic ³⁶ Cl dating	3.5–12.5
Alipoor et al. (2012)	MRF	Geological, geomorphological markers, pull-apart basins, and drainage patterns	1.6–3.2
Khorrami et al. (2019)	MRF	GNSS (regional)	2.7–4.0
Hessami et al. (2006)	Kazerun	GNSS (campaign profiles)	4–5
Walpersdorf et al. (2006)	Kazerun	GNSS (regional)	3 ± 2
Tavakoli et al. (2008)	Dena	GNSS	3 ± 2
	Kazerun		3.6 ± 0.6
Authemayou et al. (2009)	Kazerun (Northern strand)	Cosmogenic ³⁶ Cl dating	2.5–4
	Kazerun (Central strand)		1.5–3.5

Note. Adjacent fault are provided for comparison and labeled in Figure 1. Studies are ordered by year of publication.

et al., 2019; Vernant et al., 2004; Walpersdorf et al., 2006). The large variation in geological and geomorphological slip rates reflects differences in the time scales of the estimates (thousands vs. millions of years), uncertainties in the measured offsets, and uncertainties in the age of the MRF. Meanwhile, GNSS-derived estimates have suffered from the sparsity of instruments in Iran, especially in the south west and in northern Iraq. Despite these factors, there is sufficient agreement between these previous studies to strongly suggest that the fault is actively slipping at 2–6 mm/yr. The low magnitude of the slip rate, paired with the lack of any previous estimates for the locking depth, make the MRF an interesting target for InSAR.

Interferometric Synthetic Aperture Radar (InSAR) time series analysis is a well-established technique for measuring ground deformation linked to interseismic strain accumulation (Biggs & Wright, 2020; Fialko, 2006; Hussain, Hooper, et al., 2016; Jolivet et al., 2013; Tong et al., 2013; Weiss et al., 2020), and has been shown in a couple of instances to be able to estimate interseismic fault slip rates down to a few millimeters per year (Bell et al., 2011; Mousavi et al., 2015). The European Space Agency's (ESA) Sentinel-1 C-band SAR satellites provide previously unprecedented temporal coverage of data suitable for interferometry, with all of Iran being imaged on average every 6 days. Current sensing limits for InSAR time series methods are 2–3 mm/yr for an average point velocity, given a large number (hundreds) of acquisitions over a long time period (several years) and in the presence of minimal noise (Morishita et al., 2020). The total time period covered has a greater influence on the sensing threshold than the number of images used (Morishita et al., 2020). Iran is generally a suitable target location for InSAR, given its relatively arid climate and sparse vegetation cover. InSAR time series methods have been applied to measure interseismic slip rates on a number of faults in the region, including the Ashkabad (5–12 mm/yr; Walters et al., 2013), Doruneh (2.5 ± 0.3 mm/yr; Mousavi et al., 2021), North Tabriz (6–10 mm/yr; Aghajany et al., 2017; Karimzadeh et al., 2013; Rizza et al., 2013; Su et al., 2016), Shahroud (4.75 ± 0.8 mm/yr; Mousavi et al., 2015), and the Minab-Zendan-Palami (10 mm/yr) and Sabzevaran-Kahnuj-Jiroft (7.4 mm/yr) fault systems (Peyret et al., 2009). However, InSAR has not previously been used to estimate the interseismic motion across the MRF, despite the potential of this technique to better constrain both the slip rate and locking depth of this important fault. This reflects both the magnitude of the signal, and the non-optimal strike of the MRF (300°–315°) which produces a significant North-South component of motion to which InSAR is relatively insensitive.

Using ESA's Sentinel-1 SAR satellites and 5.5 years of data covering a 400 × 200 km area centered on the MRF, we measure the relative horizontal motion in a velocity time series to the millimeter per year level. We mitigate atmospheric noise contamination and co- and post-seismic signals for the M_w 7.3 Sarpol-e Zahab earthquake in

2017, and from these corrected velocity data we investigate the fault kinematics of the MRF, namely the rate of interseismic fault slip and the depth above which the fault is considered locked, using a simple screw dislocation model (Savage & Burford, 1973) and following a Bayesian framework to assess the uncertainties based upon the data noise. We conclude with a discussion of the role of the MRF in accommodating convergence between the Arabian and Eurasian plates, the extent of slip localisation, and the limitations of measuring tectonic signals close to the current sensing limit of Sentinel-1 InSAR observations.

2. Tectonic Background

Iran constitutes one of the widest zones of continental convergence on a global scale (Allen et al., 2004, 2013). Present day convergence rates between Arabia and Eurasia are estimated at 15–25 mm/yr (Khorrami et al., 2019; McClusky et al., 2003; Figure 1c). Convergence is roughly range-perpendicular in the southeastern Zagros, becoming increasingly oblique up to 45° in the northwest. Talebian and Jackson (2004) first suggested that deformation in the western Zagros is partitioned into range-perpendicular shortening and range-parallel strike-slip motion, later supported by Iranian GNSS velocity fields (Khorrami et al., 2019; Walpersdorf et al., 2006) and crustal stress maps (Zarifi et al., 2014). Some faults do still exhibit significant oblique slip, such as during the Sarpol-e Zahab earthquake (Nissen et al., 2019). At longitudes between 48°E and 55°E, 7–10 mm/yr of shortening is accommodated by range-perpendicular movement on thrust faults (Khorrami et al., 2019; Vernant et al., 2004; Walpersdorf et al., 2006). This decreases to 4–6 mm/yr moving westward to 42°E–46°E.

The Zagros is also one of the most seismically active fold-and-thrust belts in the world (Hatzfeld & Molnar, 2010; Hatzfeld et al., 2010; Nissen et al., 2011; Talebian & Jackson, 2004; Figure 1a). Focal depths generally range between 4 and 25 km, with the majority failing to rupture to the surface (Karasözen et al., 2019). While earthquakes nucleate in both the basement and sedimentary cover in similar proportions (Karasözen et al., 2019), the majority of moderate-sized earthquakes (M_w 5–6) occur within the lower sedimentary cover between depths of 5–10 km (Nissen et al., 2011). Seismicity accounts for around half of the geodetic shortening rate in the northwestern Zagros, and less than a third in the southeast, implying large amounts of folding, aseismic fault slip, and ductile shortening of the basement (Karasözen et al., 2019; Masson et al., 2005). Rates of seismicity drop off rapidly northwest of the MRF in the Central Iranian Plateau.

The Main Recent Fault trends NW-SE for over 800 km as a linear series of fault segments (numbered in Figure 1a). These segments may be characterized by their strike, which changes from 330° northwest of Kamyaran, to 300° in the center near Sahneh, and 315° southeast of Borujerd (Talebian & Jackson, 2002). The overall slip vector is believed to be parallel to the central section (47°E–50°E), between 300° and 310°, suggesting oblique motion on both northwestern and southeastern segments. The MRF cross-cuts the Main Zagros Thrust Fault (MZTF), having partially inherited its fault trace west of 49°E (Tchalenko & Braud, 1974). The MZTF traces the suture between the Arabian margin and the Iranian block and is currently thought to be inactive (Walpersdorf et al., 2006). Relocated seismic events by Ghods et al. (2012) highlighted slip on previously unmapped faults, suggesting continuing evolution of the geometry of the MRF. The MRF contains multiple pull-apart basins (Authemayou et al., 2009; Sepahvand et al., 2012; Talebian & Jackson, 2002), related either to the change in strike (Talebian & Jackson, 2002) or the changing convergence direction (Copley & Jackson, 2006). To the southeast, the MRF terminates in a “horse tail” structure formed by the Dena, Kazerun, Borazjan, Kareh Bas, and Sarvestan faults (Authemayou et al., 2009; Bachmanov et al., 2004; Khorrami et al., 2019). To the northwest, right-lateral motion continues into a complex dextral shear zone that runs along the Arabian-Eurasian suture north of 37°N (Niassarifard et al., 2021). This in turn joins two NNW-striking normal fault zones north of 37.5°N, which accommodate range-parallel motion through ESE-extension. Right-lateral strike-slip motion is resumed on the North Tabriz Fault in NW Iran (Aghajany et al., 2017) and the North Anatolian fault in Turkey (Hussain, Hooper, et al., 2016).

Calibrated earthquake relocations from Karasözen et al. (2019) show that the majority of earthquakes close to the MRF occur at depths shallower than 15 km. A minority of events are recorded at depths closer to 20 km, implying a likely locking depth of around 15–20 km. The 2006 Silakhour sequence, consisting of two foreshocks on the 30th March (M_b 4.8 and 5.2) and a M_w 6.1 mainshock on the 31st March, ruptured two patches of the MRF (Ghods et al., 2012; Peyret et al., 2008). These patches were on the western Nahavand-Borujerd and eastern Borujerd-Dorud segments, separated by 10 km of fault that did not rupture. The Nahavand-Borujerd patch was not

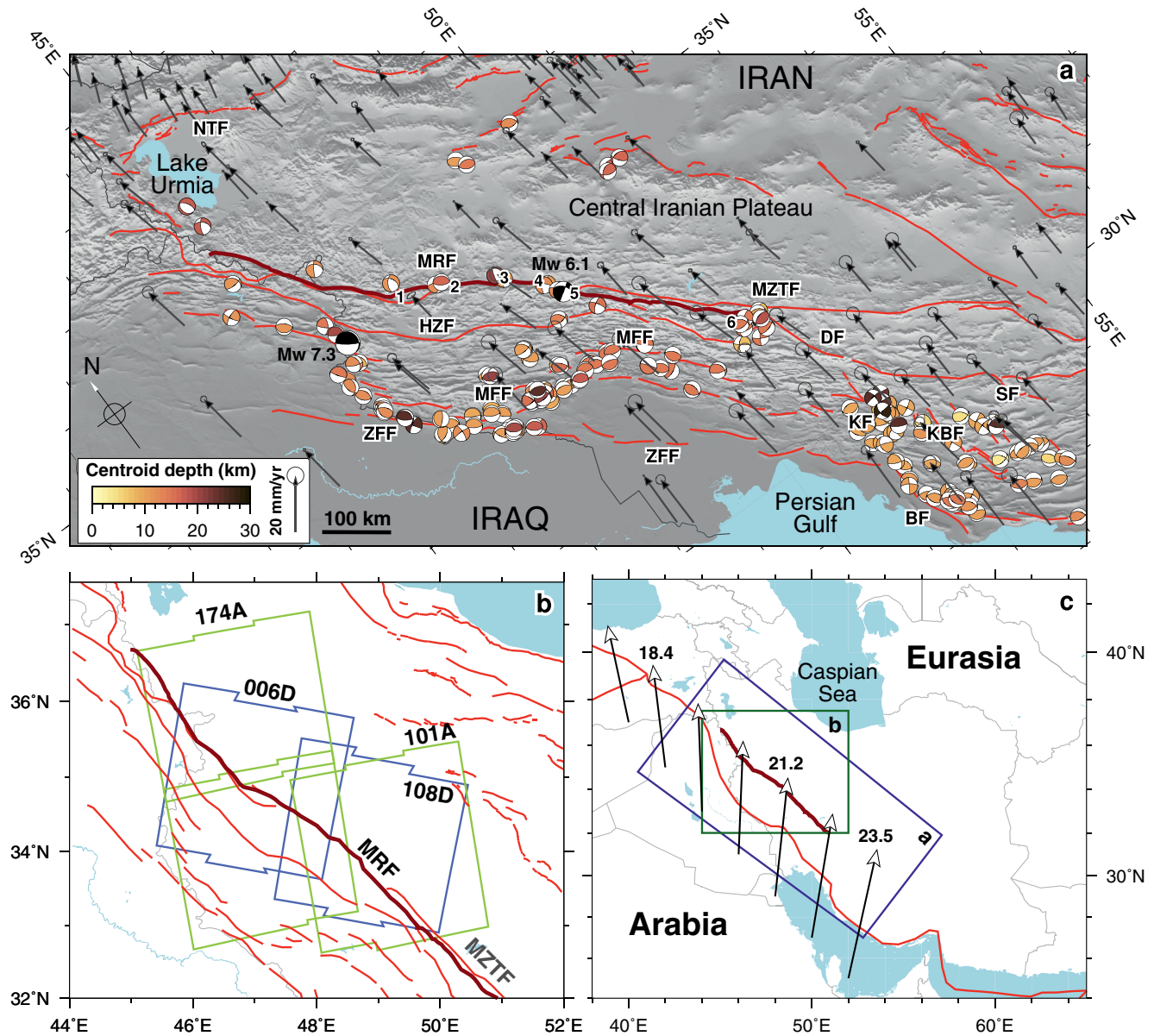


Figure 1. Overview of the study area in Western Iran. (a) Location of major faults (red lines) from Walker et al. (2010), with a 750 km section of the MRF highlighted in dark red. Vectors show GNSS velocities with 1σ uncertainties from Khorrami et al. (2019) with respect to a stable Eurasia. Focal mechanisms show relocated seismicity from Karasözen et al. (2019) covering 1962–2017, colored by hypocenter depth. From West to East: NTF = North Tabriz Fault, ZFF = Zagros Foredeep Fault, HZF = High Zagros Fault, MRF = Main Recent Fault, MFF = Mountain Front Fault, MZTF = Main Zagros Thrust Fault, DF = Dena Fault, KF = Kazerun Fault, BF = Borazjan Fault, KBF = Karih Bas Fault, SF = Sarvestan Fault. Fault segments are numbered as: 1, Kamyanan; 2, Sahneh; 3, Nahavand; 4, Borujerd; 5, Dorud; 6, Ardal. (b) LiCS defined frames for Sentinel-1 InSAR coverage. A = Ascending orbital track, D = Descending orbital track. Focal mechanisms are shown for the M_w 7.3 2017 Sarpol-e Zahab mainshock (Nissen et al., 2019) and the M_w 6.1 2006 Silakhour mainshock (Ghods et al., 2012). (c) Plate boundary from Bird (2003) shown in red, Arabian plate velocities (mm/yr) relative to stable Eurasia (Kreemer et al., 2014).

associated with any known fault structure, suggesting ongoing development of the fault zone (Ghods et al., 2012). The largest historical earthquake believed to have occurred on the fault, a M_s 7.4 earthquake near Dorud in 1909, ruptured 45–65 km of the fault (Ambraseys & Moinfar, 1973).

Large earthquakes have also occurred on adjacent faults, including the M_w 7.3 Sarpol-e Zahab earthquake in 2017 (Barnhart et al., 2018; Nissen et al., 2019; K. Wang & Bürgmann, 2020) which ruptured a dextral-thrust fault beneath the Lurestan arc, 100–200 km south of the MRF. Ground surface deformation from the earthquake may be observable up to the MRF, which would constitute a source of error in our velocity estimates. The oblique slip

Table 2
Time Extent and Number of Processed SAR Data for Each Track Used in This Study

Track	Start	End	Duration (yr)	No. of epochs	No. of ifgs generated	No. of ifgs used	Mean ifg length (d)
006D	2014-10-06	2020-07-06	5.75	196	1022	997	10.8
108D	2014-10-25	2020-07-13	5.72	204	1024	987	10.3
174A-N	2014-11-10	2020-06-23	5.62	219	984	939	9.5
174A-S	2014-11-10	2020-06-23	5.62	206	884	878	10.0
101A	2015-02-09	2020-07-06	5.41	213	720	665	9.3

Note. A = ascending orbital tracks (acquisition time 14:43–14:52 UTC, 18:13–18:22 IRST, 19:13–19:22 IRDT), D = descending orbital tracks (acquisition time 02:45–02:52 UTC, 06:15–06:22 IRST, 07:15–07:22 IRDT). Typically about 200 SAR images are used to produce 700–1000 interferograms (ifgs) (no. of ifgs generated) spanning a 6–12 day period (10 days on average), which are then reduced in number by various quality checks (no. of ifgs used). 174A-N and 174A-S refer to the northern and southern frames shown in Figure 1b, respectively. UTC = Coordinated Universal Time, IRST = Iranian Standard Time, IRDT = Iranian Daylight Time.

direction highlights the incomplete partitioning of convergence onto reverse and strike-slip faults in the western Zagros. Similarly, the 2008 and 2012 Moosiyani earthquake sequences, which occurred on the Zagros foredeep fault, caused seismic and aseismic strike-slip motion on structures other than the MRF (Nippres et al., 2017). An accurate interseismic slip rate for the MRF will allow for an improved assessment of the degree of strain localisation and partitioning on the MRF. A measurable vertical velocity contrast across the MRF would suggest dip-slip motion and incomplete partitioning. A lower slip rate than is required to accommodate the plate motion velocity contrast across the Zagros may suggest more distributed slip across adjacent faults, or a significant component of off-fault deformation.

3. Methods

3.1. InSAR Processing

We process a total of 1038 Sentinel-1 Interferometric Wide Swath images across two ascending tracks (174 and 101) and two descending tracks (006 and 108), with an average time span of 5.6 years from late 2014 to mid 2020 (Table 2). From these images, we produce a total of 4634 interferograms. Interferograms are formed between each acquisition and the three previous epochs to form a redundant network with minimized temporal baselines (Figure S1 in Supporting Information S1). Additionally, we produced long temporal baseline interferograms to bridge periods of low coherence (e.g., winter). We manually remove a total of 52 interferograms that failed to generate correctly due to processing errors.

We generate interferograms using the LiCSAR system, a set of high-level tools and algorithms that operate the GAMMA SAR and Interferometry software (Wegmüller et al., 2016; Werner et al., 2000). The reader is referred to Lazecky et al. (2020) for an in-depth description of the processing system. Images are processed in predefined frames that average 13 bursts across each of the three subswaths that were acquired in Terrain Observation with Progressive Scans (TOPS) mode. We remove topographic contributions to the phase return using the 1 arc-second SRTM DEM (Farr et al., 2007). We unwrap each interferogram in two dimensions using the statistical-cost network-flow algorithm (SNAPHU) version 2 (Chen & Zebker, 2000, 2001, 2002). Interferograms are multi-looked by 20 in range and 4 in azimuth (46.6×55.9 m) during the processing, and then further downsampled to 100×100 m pixels outside of GAMMA.

Atmospheric noise is often the largest source of error in InSAR data and results from spatially-correlated radar path delays as waves are refracted through the troposphere (Parker et al., 2015; Zebker et al., 1997). We mitigate this error using the Generic Atmospheric Correction Online Service for InSAR (GACOS) (Yu et al., 2017; Yu, Li, & Penna, 2018; Yu, Li, Penna, & Crippa, 2018), which provides tropospheric delay maps derived from the European Centre for Medium-Range Weather Forecasts (ECMWF) upscaled through use of a DEM. These maps include both hydrostatic and wet components. ECMWF models are provided every 6 hours and can be interpolated to any SAR acquisition time in between. For each interferogram, the respective tropospheric zenith delay maps are differenced, projected into the satellite line-of-sight (LOS), and then subtracted from the interferogram.

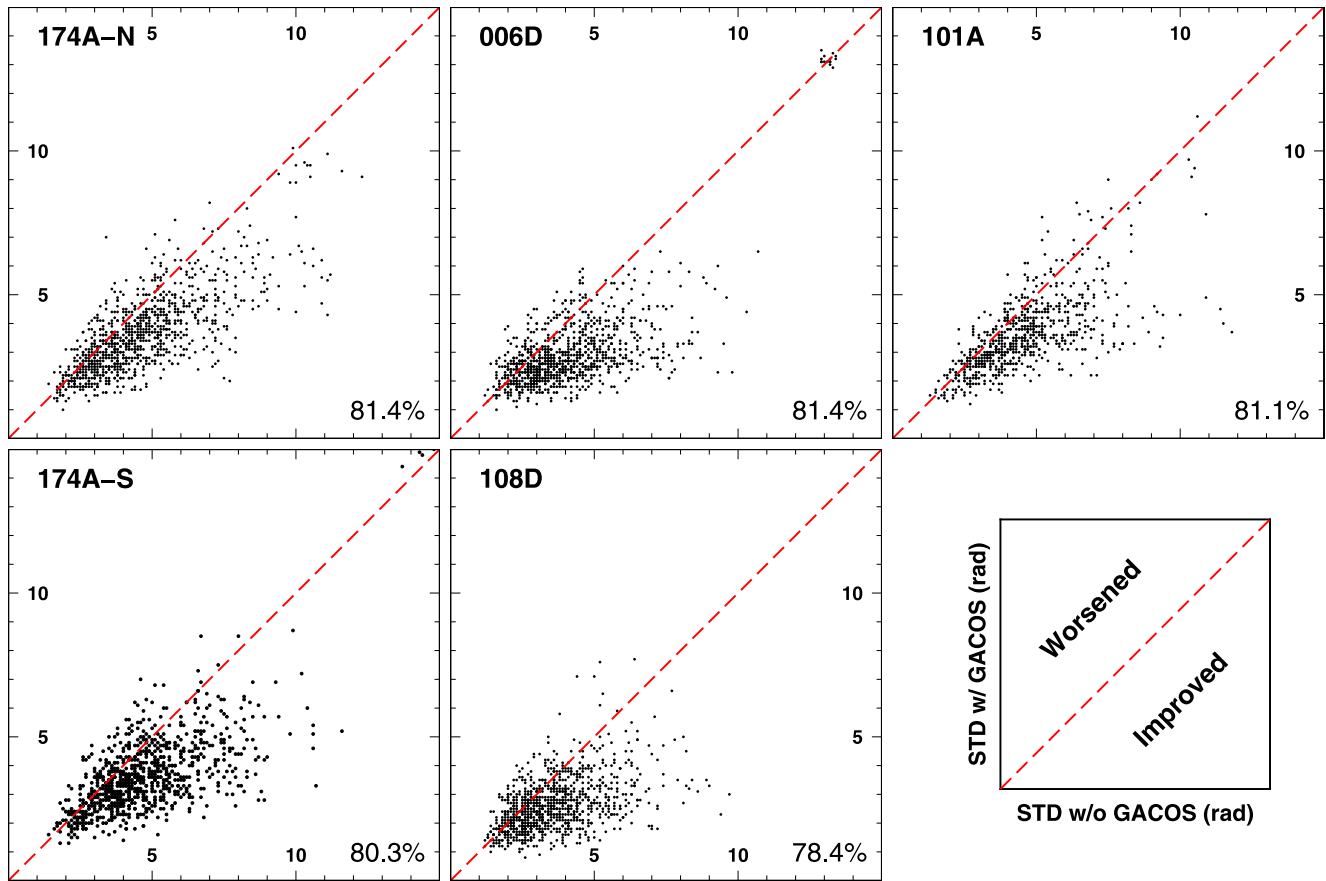


Figure 2. Change in the standard deviation (SD) of all pixels in each interferogram resulting from the application of the GACOS correction. Each black dot represents an interferogram, with black dots below the red dashed line indicating an improvement in terms of interferogram noise from the application of the atmospheric model. The percentage of interferograms showing a reduction in SD for each frame is given in the bottom right of each subpanel. The distinct high SD clusters seen in 006D and 174A-S are associated with the M_w 7.3 earthquake.

Figure 2 shows the change in the standard deviation of each interferogram after the GACOS correction has been applied. On average, 81% of interferograms for each frame show a decrease in the standard deviation, associated with a reduction in atmospheric noise, following the application of the GACOS correction, assuming that no tectonic signal is visible in the short time span interferograms.

Next, we use LiCSBAS, a small-baseline time-series analysis package, to generate cumulative line-of-sight displacements and average velocities from our interferograms (Morishita, 2021; Morishita et al., 2020). Morishita et al. (2020) provide an in-depth explanation of the software, which we summarize below. We further downsample our 100×100 m interferograms to 1 km to reduce processing requirements while retaining sufficient resolution to capture short-wavelength tectonic signals. Interferograms with low average coherence (<0.05) and which cover less than 30% of the LiCSAR frame are identified and removed. The coverage check is required because the Sentinel-1 Single Look Complex images distributed by ESA may not cover the entire LiCSAR frame. We identify phase unwrapping errors by calculating the loop closure phase, Φ of every interconnected image triplet following Equation 1 (Biggs et al., 2007):

$$\Phi_{123} = \phi_{12} + \phi_{23} - \phi_{13} \quad (1)$$

where ϕ_{12} , ϕ_{23} , and ϕ_{13} are the interferograms formed from SAR images ϕ_1 , ϕ_2 , and ϕ_3 . Near-zero values of Φ for a triplet indicate that the unwrapping is consistent between all three interferograms, while values near integer multiples of 2π indicate the presence of unwrapping errors in at least one interferogram. We calculate the root mean square (RMS) of the loop closure phase image for every triplet and remove a total of 116 interferograms where the RMS is greater than 1.5 rad for every loop that the interferogram is a part of. Cumulative

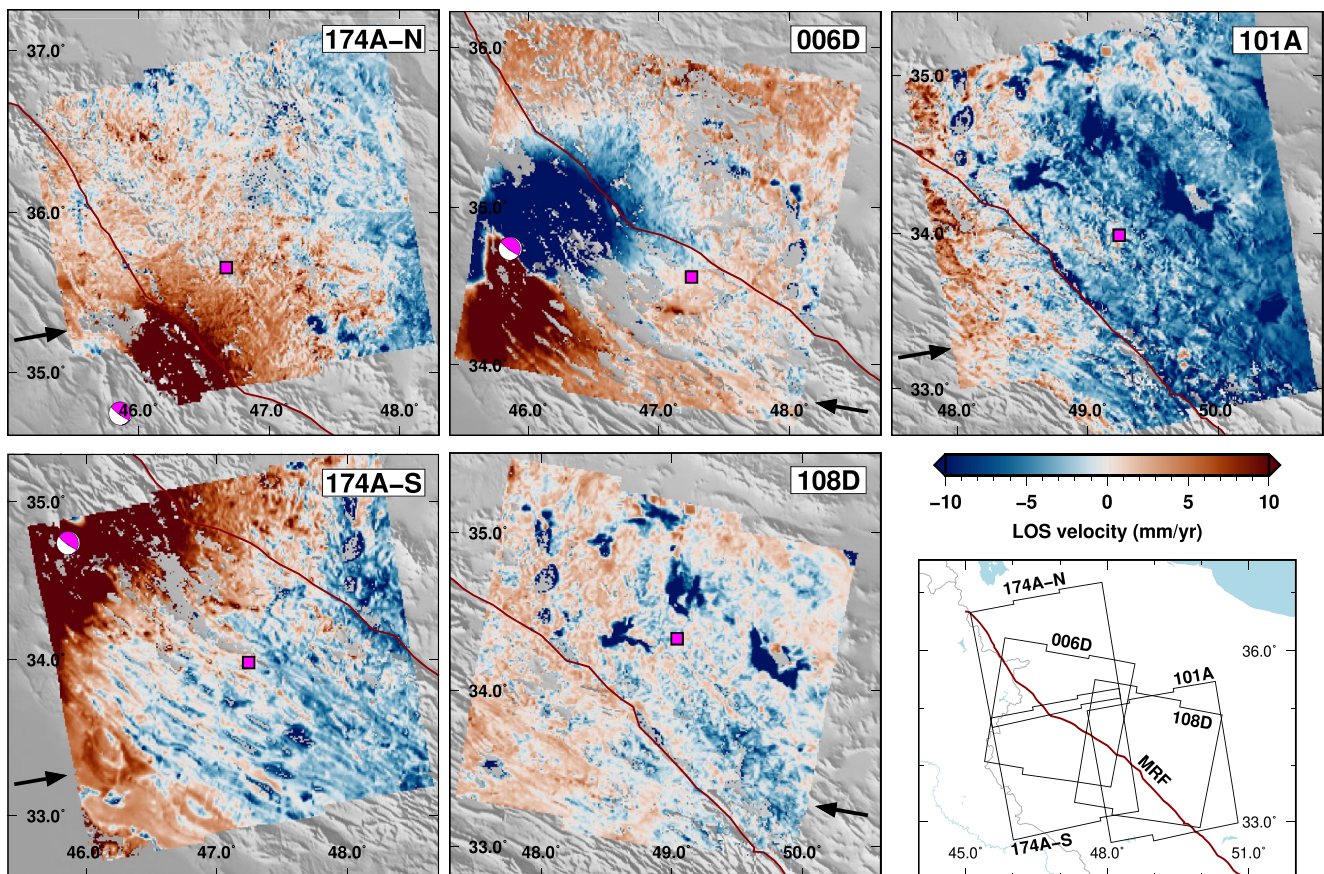


Figure 3. Average line-of-sight velocities for ascending and descending tracks at 1 km resolution. Black arrows show the horizontal projection of the LOS vector. Red and blue indicate motion toward and away from the satellite, respectively, relative to a reference pixel (pink squares). The effect of the M_w 7.3 2017 Sarpol-e Zahab mainshock (pink focal mechanism) is clearly visible in frames 174A-N, 174A-S and 006D as the large positive and negative velocity areas saturated in this image. A number of subsiding basins are visible as regions with rates faster than -10 mm/yr.

LOS displacements are inverted for a linear velocity on a pixel-by-pixel basis following the NSBAS least-squares method (Doin et al., 2011), using the 4466 interferograms that passed the quality checks. In the case of missing observations in the displacement time series (e.g., incoherence, missing acquisitions), LiCSBAS imposes a linear temporal constraint across the gap. These estimated displacements may be unreliable if the network gap is large and the displacement series deviates significantly from a linear function. Therefore, we generate additional interferograms to ensure there are no breaks in our small-baseline networks, and mask any points with gaps in their displacement series. Gaps in the displacement series can occur even when the small-baseline network is fully connected if points are missing from individual interferograms (e.g., incoherence). The average velocities are referenced to a stable pixel in each frame, chosen by calculating the RMS of all the loop closure phases for each pixel and selecting the lowest, with the requirement that the pixel must be unmasked in every interferogram. We estimate the uncertainty on the velocities by applying the percentile bootstrap method (Efron & Tibshirani, 1986) to the cumulative displacements for each pixel. Each displacement series is randomly resampled with data replacement 100 times and the velocity is re-calculated. The standard deviation of the final 100 velocities is taken as the uncertainty on the LOS velocity. A number of statistical quality checks (Morishita et al., 2020) are used to threshold a mask for the velocity map (Introduction of the Supporting Information, Figures S2–S7 in Supporting Information S1). The LOS velocity maps for each frame are shown in Figure 3. Example displacement series for two pixels, one across-fault difference and one subsidence signal, are shown in Figures S8 and S9 in Supporting Information S1.

3.2. Evaluation of Co- and Post-Seismic Signals

Tracks 174A and 006D span (both spatially and temporally) the November 12, 2017 M_w 7.3 Sarpol-e Zahab earthquake (Nissen et al., 2019) and subsequent aftershock sequences (Lv et al., 2020). The earthquake involved dextral-thrust slip on a 40×20 km basement fault in the Lurestan arc, potentially triggering aftershocks up to 80 km away. Displacements of up to 90 cm in LOS were observed in Sentinel-1 interferograms spanning the event (Nissen et al., 2019). The first main aftershock sequence occurred on January 11, 2018, consisting of five events between M_w 5.1–5.5 (Lv et al., 2020). The second occurred on November 25, 2018 and consisted of M_w 6.3, 5.2, and 5.0 events. In the 1 year period following the mainshock, an additional 100 mm of LOS displacement was observed related to postseismic deformation (K. Wang & Bürgmann, 2020). For areas affected by the Sarpol-e Zahab earthquake, any estimate of the interseismic slip rate will be biased by the co- and post-seismic displacements (Figure 3). A full assessment of the magnitude and spatial extent of these signals in the InSAR velocity field is required so as to be able to robustly estimate the interseismic slip rate.

We first attempt to mitigate the coseismic signals by forwarding modeling the displacements and subtracting these from the cumulative displacements generated by LiCSBAS. For the mainshock, we use fault parameters estimated by Nissen et al. (2019) from Sentinel-1 interferograms and a uniform slip fault model (Table S1 in Supporting Information S1). We model both aftershock sequences as a single event using InSAR-derived fault parameters from Lv et al. (2020). The fault is modeled using a rectangular dislocation source (Okada, 1985) defined by nine parameters: x-position, y-position, strike, dip, rake, slip, fault length, top depth, and bottom depth. We chose InSAR-derived fault parameters, as opposed to those from seismology, as they may more accurately fit our own observed InSAR signals. Modeled surface displacements are projected into the satellite LOS for each frame and then removed from the cumulative displacement series produced by LiCSBAS. We then use LiCSBAS to re-estimate the average LOS velocity for these three frames using the updated displacement series.

Next, we calculate the change in the average LOS velocity following the November 12, 2017 M_w 7.3 mainshock. To do this, we split the cumulative displacement time series produced by LiCSBAS into two parts about November 12, 2017 and solve for the average velocity pre- and post-earthquake using least squares. We do not attempt to remove the post-seismic signal from the times series (K. Wang & Bürgmann, 2020), as the signal is difficult to separate from the noise and any errors could be of a similar magnitude to the interseismic signal. Points for which the average velocity changed significantly following the earthquake may have been affected by post-seismic deformation. The reduction in time series length to 2–3 years either side of the earthquake will increase the velocity uncertainties to 4–5 mm/yr (Morishita et al., 2020). Additionally, the time series before the earthquake contains fewer interferograms because Sentinel-1B was inactive for some of this time period (2014–2017). We calculate the velocity difference for the three affected frames and combine them by averaging overlapping pixels. We estimate the expected velocity difference as a result of noise and non-tectonic signals by calculating the velocity difference for 108D, which should be unaffected by the Sarpol-e Zahab earthquake sequence. We calculate a standard deviation of 11.4 mm/yr from all pixels within frame 108D, and contour the merged velocity differences based on the 95% confidence interval. Figure 4 shows the merged and contoured velocity differences for frames 006D, 174A-N, and 174A-S. The primary post-seismic signal is highlighted by the pink square and covers an area of approximately 100×150 km. We observe a similar spatial extent to the cumulative post-seismic displacements observed by K. Wang and Bürgmann (2020, Figure 4). The true extent of the post-seismic deformation likely extends further than the highlighted area, given the uncertainty in our velocities and the threshold used, and so we avoid velocities west of 47°E when selecting profile lines.

3.3. Velocity Field Generation

Our initial LOS InSAR velocity fields are referenced relative to a stable pixel for each frame (pink squares in Figure 3). To better combine all four tracks, we shift the LOS velocities into a Eurasia-fixed reference frame (Hussain, Hooper, et al., 2016; Hussain et al., 2018; Weiss et al., 2020). Using horizontal GNSS velocities provided by Khorrami et al. (2019), we fit second-order polynomial surfaces to the East and North velocity components within one degree of our study area (Figure 5). The velocities are weighted using their respective bootstrapped uncertainties. We then project the GNSS velocity fields into the satellite LOS for each frame. To minimize the impact of short-wavelength and transient signals on our referencing, namely those from groundwater subsidence and the Sarpol-e Zahab earthquake, we temporarily mask any InSAR velocities outside of one standard deviation. We calculate the residual between the projected GNSS velocities and the InSAR velocities, and fit a second-order

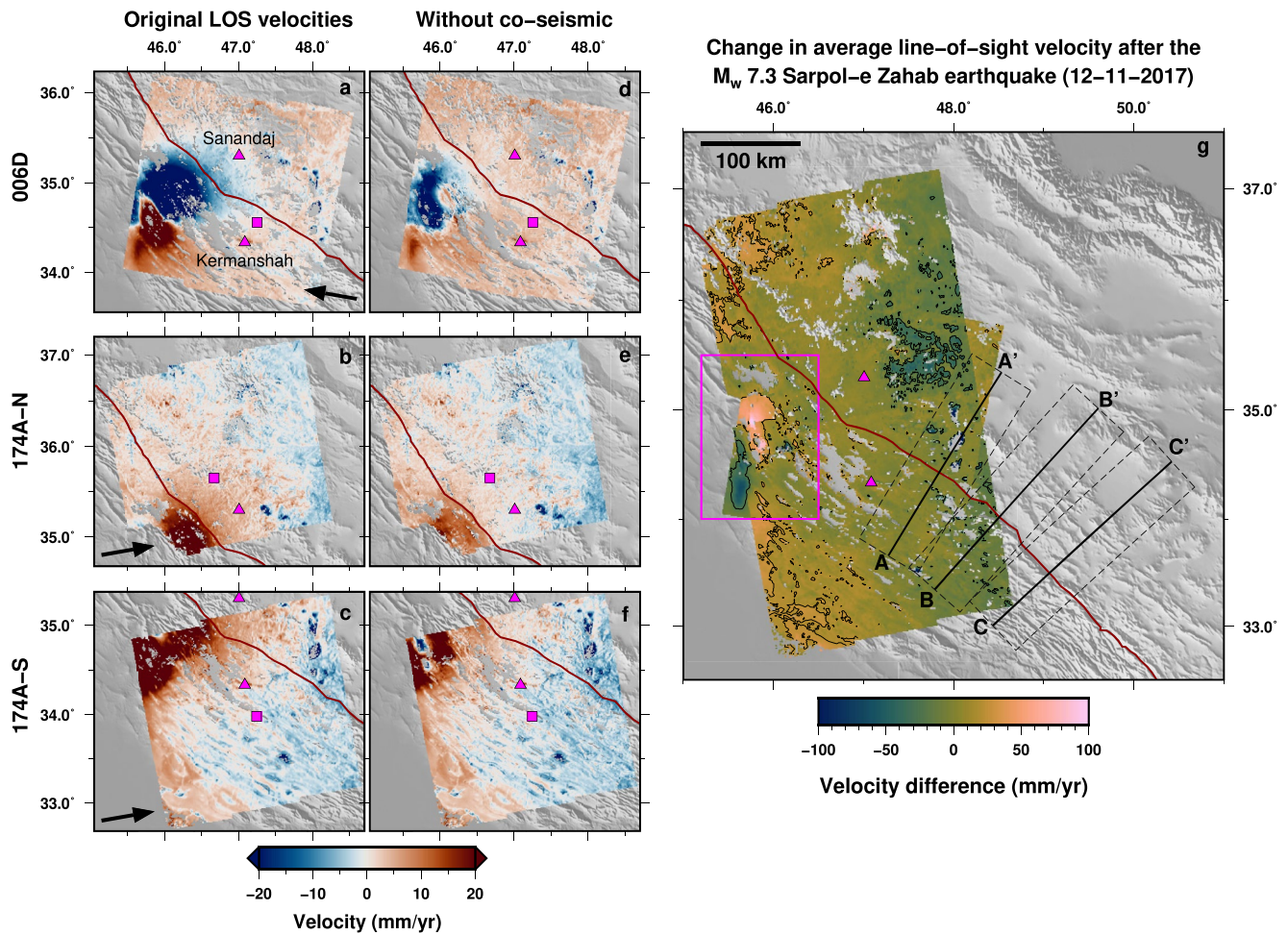


Figure 4. Analysis of co- and post-seismic signals following the M_w 7.3 2017 Sarpol-e Zahab earthquake sequence. (a–c) Original line-of-sight velocities for frames 006D, 174A-N, and 174A-S, relative to the reference pixel (pink square). Two cities, Sanandaj and Kermanshah, are marked as pink triangles for spatial reference, along with the trace of the MRF (red). Black arrows show the horizontal projection of the LOS vector. (d–f) LOS velocities after the forward models for the earthquakes shown in Table S1 in Supporting Information S1 have been removed from the displacement time series, relative to the reference pixel (pink square). (g) Difference in average line-of-sight velocities before and after the November 12, 2017 M_w 7.3 mainshock, for frames 006D, 174A-N, and 174A-S. For overlapping pixels between frames, the values have been averaged. The values are contoured at ± 23 mm/yr, based upon the 2σ value derived from frame 108D which is unaffected by the earthquake deformation. The pink rectangle highlights the region encompassing the main post-seismic signal. We choose profiles (A–A', B–B', and C–C') that avoid areas with significant velocity changes following the earthquake.

polynomial surface to the result. Subtracting this function from the respective InSAR velocity field results in InSAR velocities in the same reference frame as the GNSS velocities. Given the diffuse nature of deformation throughout the Zagros, and the lack of three-dimensional GNSS velocities to generate a vertical velocity field, our calculated referencing polynomials may over or underestimate the required transformation. We examine potential model bias resulting from this uncertainty in Section 5.3.

To investigate interseismic slip along the MRF, we decompose our satellite LOS velocities into local geodetic coordinate velocities. The velocity for each pixel observed in the satellite LOS can be expressed as a linear combination of the East, North, and Up components:

$$V_{Los} = \begin{bmatrix} \sin(\theta)\cos(\alpha) - \sin(\theta)\sin(\alpha) - \cos(\theta) \\ V_E \\ V_N \\ V_U \end{bmatrix} \quad (2)$$

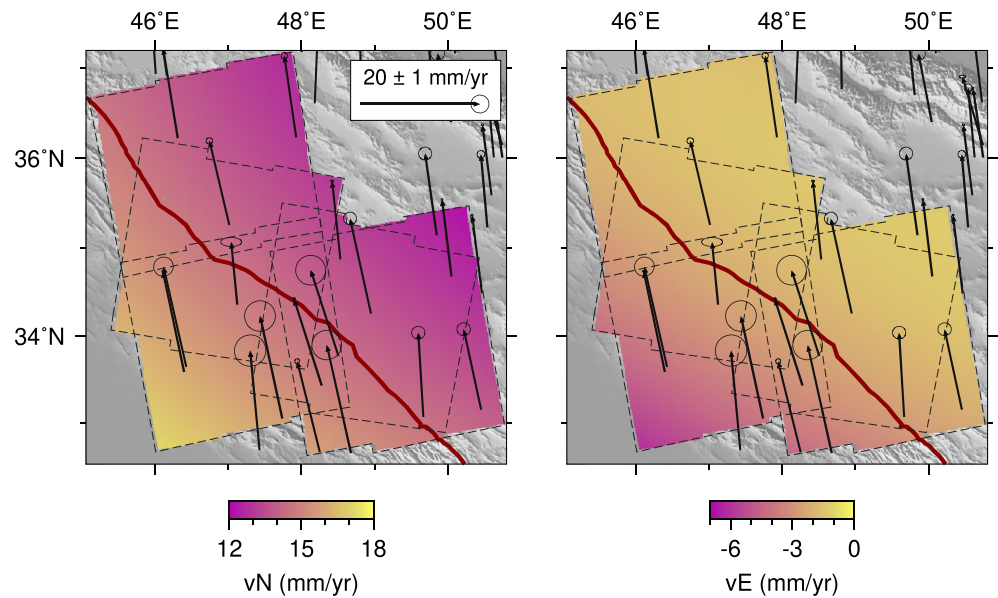


Figure 5. Spatially interpolated GNSS velocity fields generated by fitting a second-order polynomial plane to North (vN) and East (vE) GNSS velocities from Khorrami et al. (2019) relative to a stable Eurasia, cropped to the area covered by the InSAR. GNSS velocities are located at the base of the arrows and given with 1σ uncertainties.

where θ is the radar incidence angle, measured from the vertical to the LOS, and α is the azimuth of the along-track satellite heading. The majority of our study area is covered by two overlapping tracks, one ascending and one descending. In this situation, we have two observations (V_{asc} and V_{desc}) and three unknowns (V_E , V_N , and V_U), making the inverse problem under-determined. In order to find a unique solution to the problem, we must add either further observations or a-priori constraints for one of the model parameters. Sentinel-1 InSAR observations are particularly insensitive to displacement in the north-south direction, as a result of the near-polar satellite orbit and sideways look direction. We estimate the north contribution to the InSAR LOS velocities by projecting the interpolated North GNSS velocity field (Figure 5) into the respective satellite LOS for each track. This projected velocity is then subtracted from each frame, leaving LOS velocities that contain a negligible long-wavelength north-south component. For a point with observations from two look directions, the resulting simplified linear equation is given by Equation 3.

$$\begin{bmatrix} V_{asc} \\ V_{desc} \end{bmatrix} = \begin{bmatrix} -\cos(\theta_{asc}) & \sin(\theta_{asc}) \cos(\alpha_{asc}) \\ -\cos(\theta_{desc}) & \sin(\theta_{desc}) \cos(\alpha_{desc}) \end{bmatrix} \begin{bmatrix} V_U \\ V_E \end{bmatrix} \quad (3)$$

In the presence of three or more overlapping frames, we can expand the 2-by-2 matrix in Equation 3 to a n -by-2 matrix, where n is the number of overlapping frames. For example, for a point within frames 006D, 108D, and 101A (Figure 1b), Equation 3 can be expressed as:

$$\begin{bmatrix} V_{006D} \\ V_{108D} \\ V_{101A} \end{bmatrix} = \begin{bmatrix} -\cos(\theta_{006D}) & \sin(\theta_{006D}) \cos(\alpha_{006D}) \\ -\cos(\theta_{108D}) & \sin(\theta_{108D}) \cos(\alpha_{108D}) \\ -\cos(\theta_{101A}) & \sin(\theta_{101A}) \cos(\alpha_{101A}) \end{bmatrix} \begin{bmatrix} V_U \\ V_E \end{bmatrix} \quad (4)$$

where the subscript denotes the frame. We solve Equation 3 to estimate the decomposed velocities, V_U and V_E , for every point found within at least one ascending and one descending frame, using weighted least squares and the data variance-covariance matrix (VCM). The data VCM is a n -by- n matrix containing the LiCSBAS-derived variance values for a given point in each frame along the main diagonal. We assume no correlation between

each frame, so all values off of the main diagonal are equal to zero. We also calculate the model VCM following Equation 5:

$$Q_m = (G'WG)^{-1} \quad (5)$$

where Q_m is the 2-by-2 model VCM, G is the design matrix (the n -by-2 matrix in Equation 3), and W is the inverse of the data VCM. Uncertainties for the decomposed velocities (Figure S10 in Supporting Information S1) are typically in the range of 0.2–1.0 mm/yr in the East component and 0.5–1.5 mm/yr in the Up component.

3.4. Interseismic Fault Slip Modeling

We model profiles of the InSAR-derived velocities across the deforming zone by assuming that the fault can be approximated as a vertical buried 1-D screw dislocation (Savage & Burford, 1973) defined by Equation 6:

$$v_{para}(x) = \left(\frac{s}{\pi}\right) \arctan\left(\frac{x}{d}\right) + c \quad (6)$$

where $v_{para}(x)$ is the horizontal surface velocity parallel to the fault, x is the perpendicular distance from the fault, s is the interseismic slip rate, d is the locking depth, and c is a scalar offset. We calculate fault-parallel velocities from the decomposed East velocities, assuming zero fault-perpendicular motion and using the local strike within each profile. To mitigate horizontal motion associated with subsidence, we mask the decomposed East velocities with the decomposed vertical velocities using a threshold of ± 10 mm/yr. We take three 70 km wide fault-perpendicular profiles across the MRF (A-A', B-B', and C-C'), avoiding areas with post-seismic signals (Figure 4). We solve for the interseismic slip rate, the locking depth, and a scalar offset to the velocities (Equation 6), assuming strikes of 300°, 310°, and 315° for A-A', B-B', and C-C', respectively. We fix the fault location based upon the intersection of the profile lines with the fault trace from Walker et al. (2010), and apply a scalar offset to the velocities so that the profiles are centered on approximately 0 mm/yr where they intersect the fault trace.

We estimate best fit values for each model parameter by implementing an affine-invariant ensemble Markov Chain Monte Carlo (MCMC) sampler, developed by Goodman and Weare (2010). This Bayesian approach uses semi-random walks of a given number of walkers to explore the posterior probability distribution of the model, based upon known prior constraints. Solutions are ranked using the weighted misfit between observed and model velocities. It demonstrates improved performance over traditional Metropolis-Hasting algorithms, especially in the presence of complex parameter spaces (Goodman & Weare, 2010). This method has been widely used for tectonic applications (Aslan et al., 2019; Goto et al., 2019; Hussain, Hooper, et al., 2016; Hussain, Wright, et al., 2016; Szeliga & Bilham, 2017; Tesson et al., 2021). Our MCMC sampler uses 600 walkers and runs for 300,000 iterations. We remove the first 20% of solutions as burn-in, producing 48,000 valid solutions. From these we calculate the maximum a posteriori probability (MAP) solution - that is, the most likely solution based upon the prior probabilities - and uncertainties for each model parameter. We assume a uniform prior for all model parameters based upon limits of $-10 \leq s \leq 20$ (mm/yr), $1 \leq d \leq 50$ (km), and $-10 \leq c \leq 10$ (mm/yr).

To account in the inversion for the noise of the data and correlation between nearby pixels, we calculate the spatial covariance function of the data after removing tectonic and anthropogenic signals (e.g., Hussain, Hooper, et al., 2016; Weiss et al., 2020). We take a 200×200 km region of the decomposed East velocities, avoiding the post-seismic signals in the west of the study area, and mask out any pixels associated with a vertical rate greater than ± 5 mm/yr; these signals are largely correlated with basins and are likely due to groundwater subsidence (Figure S15 in Supporting Information S1). Next, we remove a first-order polynomial plane from the velocities to account for any long-wavelength ramps related to residual orbital errors, tropospheric noise, or tectonic signals. We do not attempt to directly model and remove the tectonic signal related to the MRF to avoid any circular reasoning in our choice of fault parameters. The resulting velocities contain negligible anthropogenic signals and, while some tectonic signal from the MRF will be present, the low magnitude of this signal means that these velocities are dominated by residual short-wavelength tropospheric noise. We fit an exponential radial covariance function (Hussain, Hooper, et al., 2016) to these data of the form:

$$C(r) = \sigma^2 e^{-\frac{r}{\lambda}} \quad (7)$$

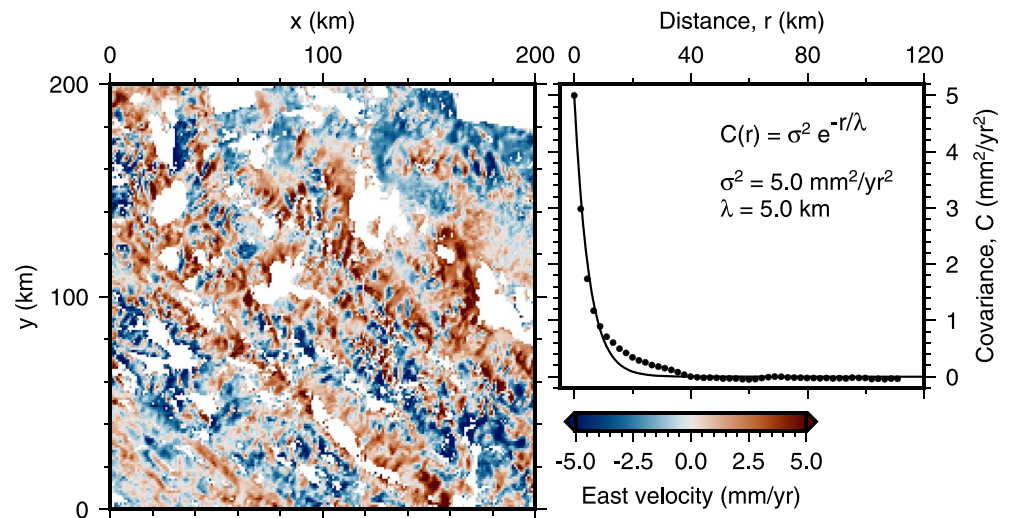


Figure 6. Autocorrelation function and best-fitting exponential (Equation 7) (right) based upon isolated non-anthropogenic noise in the East InSAR average velocities (left).

where $C(r)$ is the covariance between two velocity measurements at a distance of r , σ^2 is the variance, and λ is the exponential length scale. We solve Equation 7 for σ^2 and λ , estimating values of $5.0 \text{ mm}^2/\text{yr}^2$ and 5.0 km , respectively (Figure 6). The misfit between r values of 10–40 km, where the covariance model underestimates the observed decay in noise at mid distances, relates to asymmetry within the noise structure. This is potentially as a result of NW-SE aligned topographic structures (mountain ranges and interleaved valleys) with similar widths and lengths. We generate a variance-covariance matrix for all pixels within each profile using Equation 7 and our estimated exponential parameters, where r is the 2-D distance between pixels, and use this to weight our Bayesian inversion.

4. Results

Figure 7 shows the decomposed East, vertical, and fault-parallel velocities, the latter of which was calculated assuming a fixed strike of 310° . We observe higher velocities (red) to the northeast in both the East and fault-parallel velocities, with a velocity difference across the MRF of several millimeters per year. The velocity difference is lower west of 47.5°E where we expect the velocities to be biased by the Sarpol-e Zahab earthquake sequence (Figure 4). No equivalent velocity contrast can be seen in the vertical velocities. The large negative (blue) velocities previously observed in the LOS velocities are now only present in the vertical velocities, supporting the idea that these are subsidence signals related to groundwater extraction. This is further supported by the strong seasonality present in the displacement series for these points, which isn't present to the same magnitude in other areas (Figure S16 in Supporting Information S1).

Figure 8 shows the results of the MCMC inversion, and Figure 9 shows the marginal posterior probability distributions for each parameter. MAP solutions and uncertainties for each parameter are given in Table 3. We include the mean and standard deviation of the fault-parallel velocities (Figures 8 and 10), weighted using the variance of the East velocities (Figure S9 in Supporting Information S1) and calculated in a 10 km window moved in 1 km increments along the profiles.

Our MAP estimates of slip rate are consistent between profiles A-A' (2.3 mm/yr), B-B' (2.5 mm/yr), and C-C' (1.8 mm/yr), to within the 95% confidence intervals ($1.2\text{--}4.2$, $1.5\text{--}3.8$, and $0.8\text{--}3.9 \text{ mm/yr}$, respectively; Table 3). We see similar consistency between our MAP estimates of locking depth for profiles A-A' (12.7 km) and B-B' (13.6 km). The posterior distributions for both are either skewed (B-B') or non-Gaussian (A-A'), and so we provide the 95% interquartile range (IQR), defined as the difference between the 0.025 and 0.975 quantiles, for A-A' ($5.2\text{--}48.7 \text{ km}$) and B-B' ($5.8\text{--}48.7 \text{ km}$) as this is more representative. The upper locking depth for A-A' may also be considered unbounded, given that the distribution levels off above 20 km. Profile C-C' may be considered unbounded within the parameter range we have chosen, tending toward a very shallow locking depth.

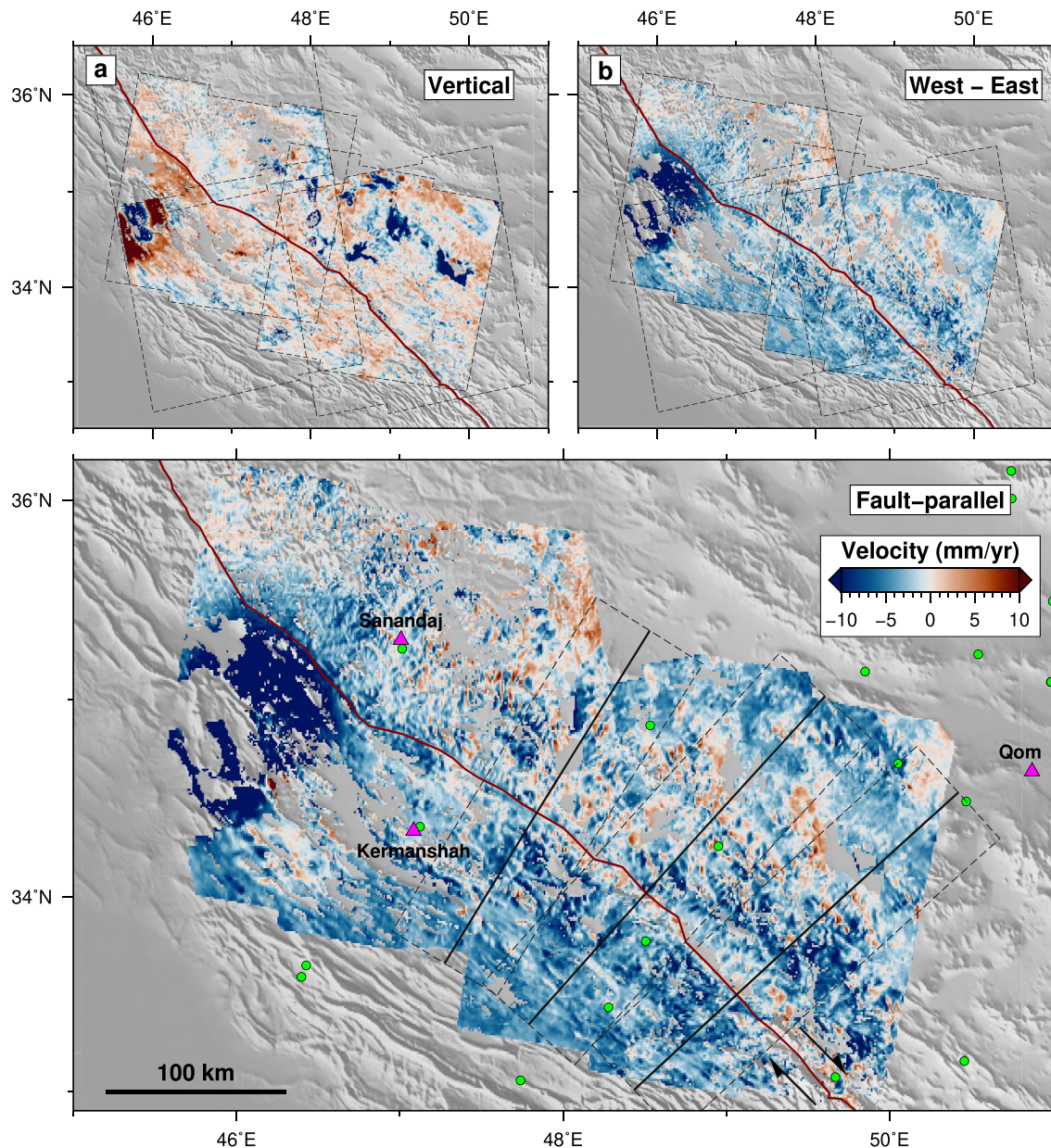


Figure 7. Decomposed Vertical (a) and East (b) velocities, and fault-parallel (c) velocities assuming an overall regional fault strike of 310° , relative to the MRF. Positive values (red) indicate motion upwards, to the east, and in a right-lateral sense, respectively. Fault-perpendicular profiles (black lines) are taken perpendicular to the projected MRF trace (red line). Velocities are overlain onto hill-shaded SRTM topography, with city locations (pink triangles) and GNSS locations (green circles) marked for reference.

All three profiles show significant noise in the observed velocities, especially profile C-C' which includes a large area of negative velocities around 40 km fault-perpendicular distance. Two potential sources of this noise are residual tropospheric noise associated with varying topography, and fading bias associated with higher vegetation cover. The underlying tectonic signal is still identifiable in profiles A-A' and B-B', although it is significantly masked in profile C-C'.

To better constrain the locking depth, we subsequently model the velocities for profiles A-A' and B-B' simultaneously. We omit profile C-C' because the estimated locking depth was unconstrained and may degrade the result. We estimate a shared locking depth across both profiles and keep separate solutions of profile-specific slip rates and offsets, otherwise repeating the previous setup. We would expect the locking depth to be approximately constant across relatively short section of a major fault. Figure 10 shows the results of the MCMC inversion,

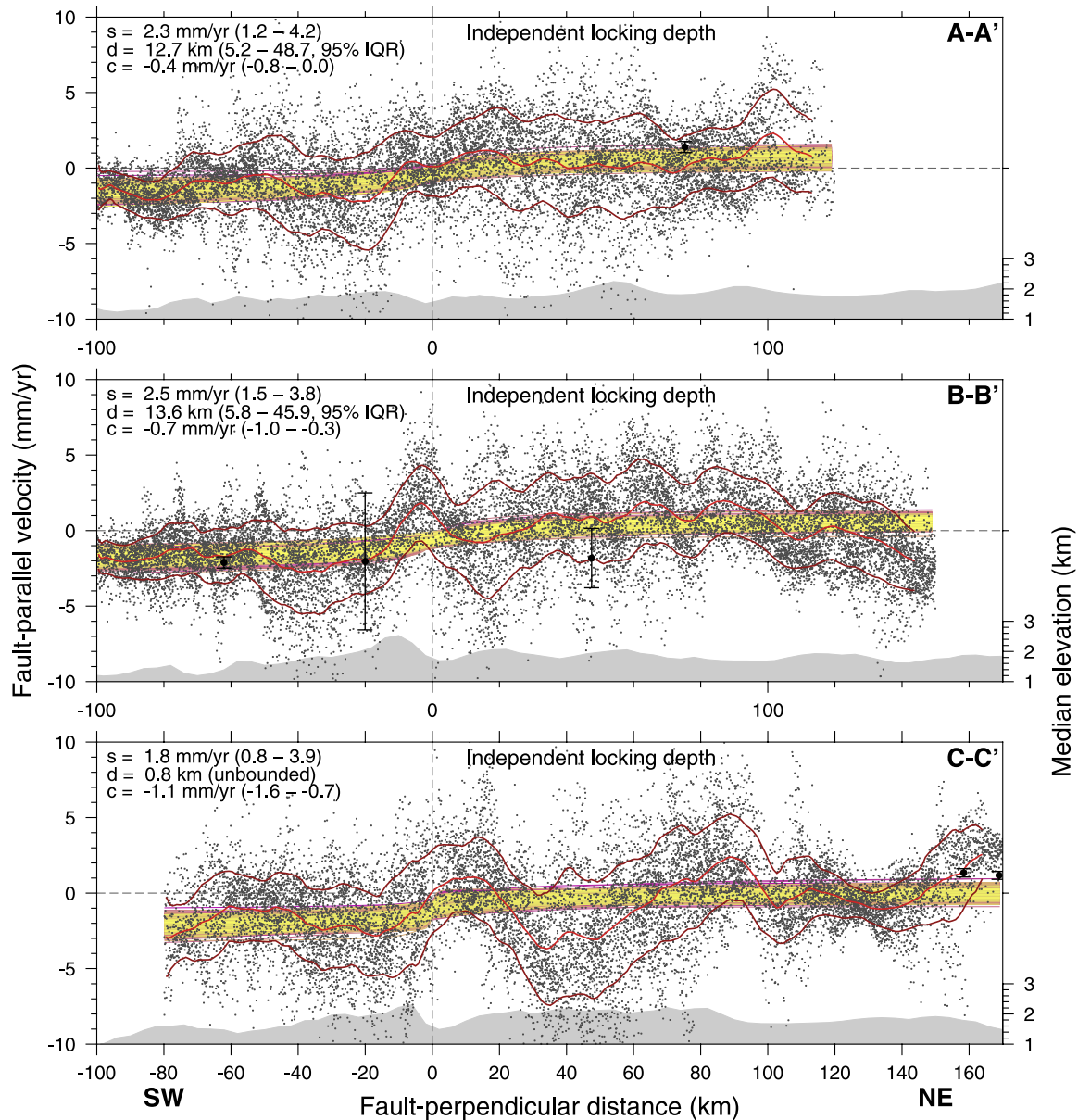


Figure 8. Northeast-southwest profiles of fault-parallel (strike direction) velocity (with positive motion to the SE shown by the black dots) relative to the surface trace of the MRF (set at zero distance), from Figure 7, modeled with independent locking depths. The light and dark red lines show the weighted average and weighted standard deviation of the velocities, respectively. A uniformly randomly selected 1% of modeled solutions are shown ranked by the posterior probability, from yellow (best) to pink (worst). The MAP solution is given in the top left of each panel with 95% confidence intervals (CI) centered on the mean, with the exception of the locking depths which are given with the 95% interquartile range (IQR) centered on the median. The median elevation and GNSS velocities within each profile are shown in gray and as black circles with error bars, respectively.

Figure 11 shows the marginal posterior probability distributions for each parameter, and Table 3 summarizes the MAP estimates and uncertainties. Our MAP estimates of slip rate are the same as the independent estimates for both profiles A-A' (2.3 mm/yr) and B-B' (2.5 mm/yr) to one decimal place, but with a shift in the 95% confidence intervals. The posterior distribution for our joint estimate of locking depth (14.1 km) has a narrower 95% interquartile range (6.1–40.2 km) than the independent estimates, and the distribution appears more Gaussian, especially compared to profile A-A'.

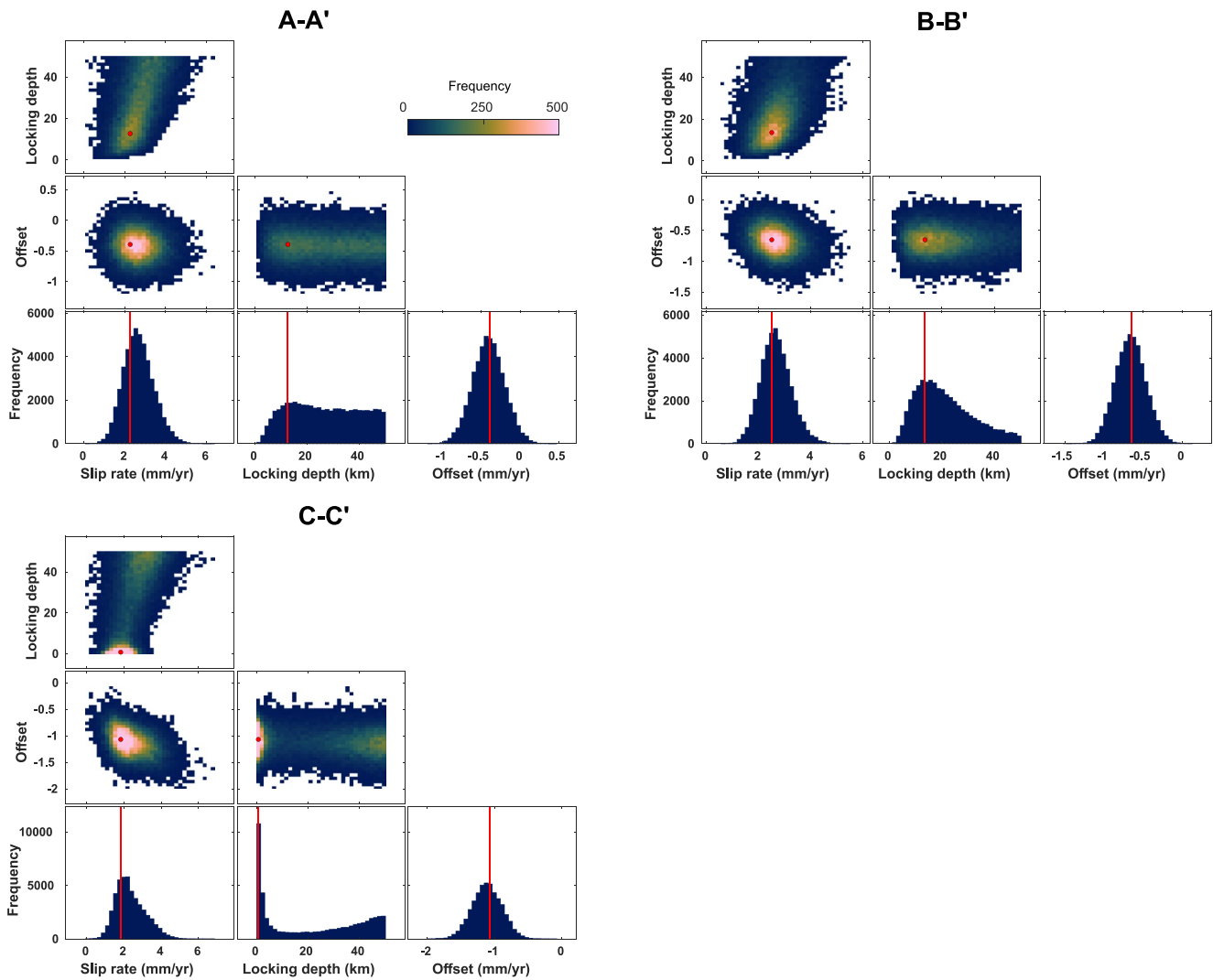


Figure 9. Marginal probability distribution for the profiles in Figure 8, including the MAP solution (red line and dot), for the MCMC inversion (48,000 solutions) under the assumption of independent slip rates, locking depths, and offsets for each profile. We assume a uniform prior for all model parameters based upon limits on the values of slip rate (−10 to 20 mm/yr), locking depth (1–50 km), and offset (−10 to 10 mm/yr).

Table 3

Maximum a Posteriori Probability Estimates and Uncertainties of the Parameters in Equation 6 for the Three Profiles Shown in Figure 7, for Both Independent (Ind) Profiles and the Two-Profile Joint Model with a Shared Locking Depth

		A-A'		B-B'		C-C'	
Ind	s (mm/yr)	2.3	(1.2–4.2)	2.5	(1.5–3.8)	1.8	(0.8–3.9)
	d (km) (95% IQR)	12.7	(5.2–48.7)	13.6	(5.8–48.7)	0.8	(unbounded)
	c (mm/yr)	−0.4	(−0.8 to 0.0)	−0.7	(−1.0 to −0.3)	−1.1	(−1.6 to −0.7)
Joint	s (mm/yr)	2.3	(1.2–3.7)	2.5	(1.4–3.7)		
	d (km)	14.1	(6.1–40.2)	14.1	(6.1–40.2)		
	c (mm/yr)	−0.4	(−0.9 to 0.1)	−0.7	(−1.1 to −0.2)		

Note. Results are given with 95% confidence intervals with the exception of the locking depths results, which are given with 95% interquantile ranges (IQR), as these distributions are significantly non-Gaussian (Figure 9).

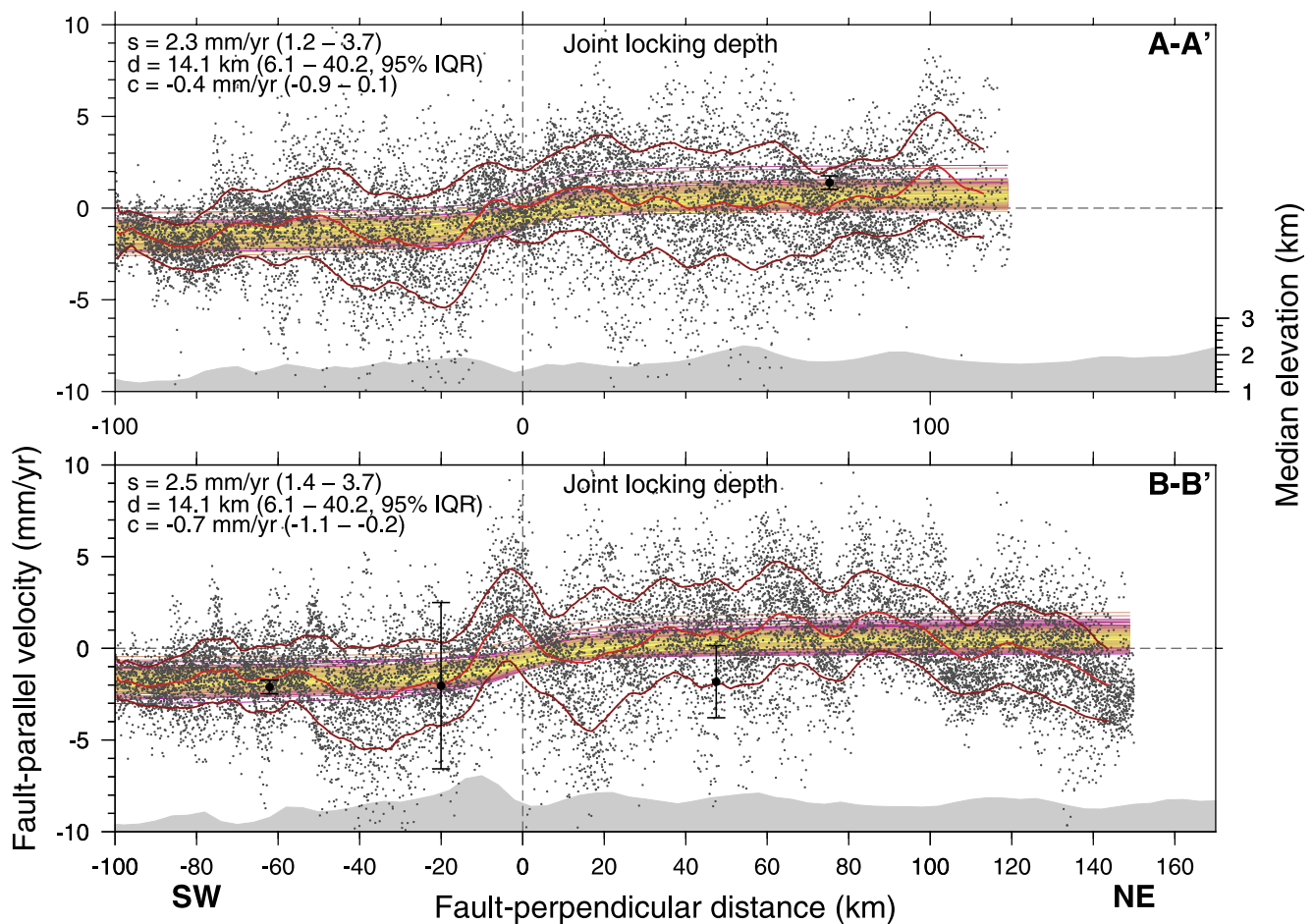


Figure 10. Northeast-southwest profiles of fault-parallel (strike direction) velocity (with positive motion to the SE shown by the black dots) relative to the surface trace of the MRF (set at zero distance), from Figure 7, modeled with a joint locking depth and individual slip rates and offsets. The light and dark red lines show the weighted average and weighted standard deviation of the velocities, respectively. A uniformly randomly selected 1% of modeled solutions are shown ranked by the posteriori probability, from yellow (best) to pink (worst). The MAP solution is given in the top left of each panel with 95% confidence intervals (CI) centered on the mean, with the exception of the locking depth which is given with the 95% interquartile range (IQR) centered on the median. The median elevation and GNSS velocities within each profile are shown in gray and as black circles with error bars, respectively.

5. Discussion

We have resolved a small rate of strain accumulation at the millimeter per year level across spatial distances of 100 km over the Main Recent Fault from 5.5 years of Sentinel-1 InSAR times series. Furthermore, we have placed geodetic bounds for the first time on the depth below which the fault is slipping in this interseismic period. Both estimates show large posterior uncertainties and are based upon a number of key assumptions which give rise to significant epistemic uncertainties. Below we compare our results to previous estimates of interseismic slip rate, discuss the model uncertainties, and also discuss challenges in constraining the locking depth for relatively noisy interseismic InSAR datasets.

5.1. Estimation of the Locking Depth

Our results provide the first InSAR-derived estimate for the locking depth of the Main Recent Fault, SW Iran. Our three estimates of locking depth from profiles A-A' (12.7 km), B-B' (13.6 km), and the joint model (14.1 km), are all clustered within a 1.4 km window, although with large uncertainties (5.2–48.7 km, 5.8–45.9 km, and 6.1–40.2 km, respectively). While the upper limit is poorly constrained for both A-A' and B-B', and C-C' is unbounded within our prior limits, we show that a joint inversion of multiple along-strike profiles with variable strike angles can better constrain the locking depth, both in terms of the upper bound and the width of the uncertainties.

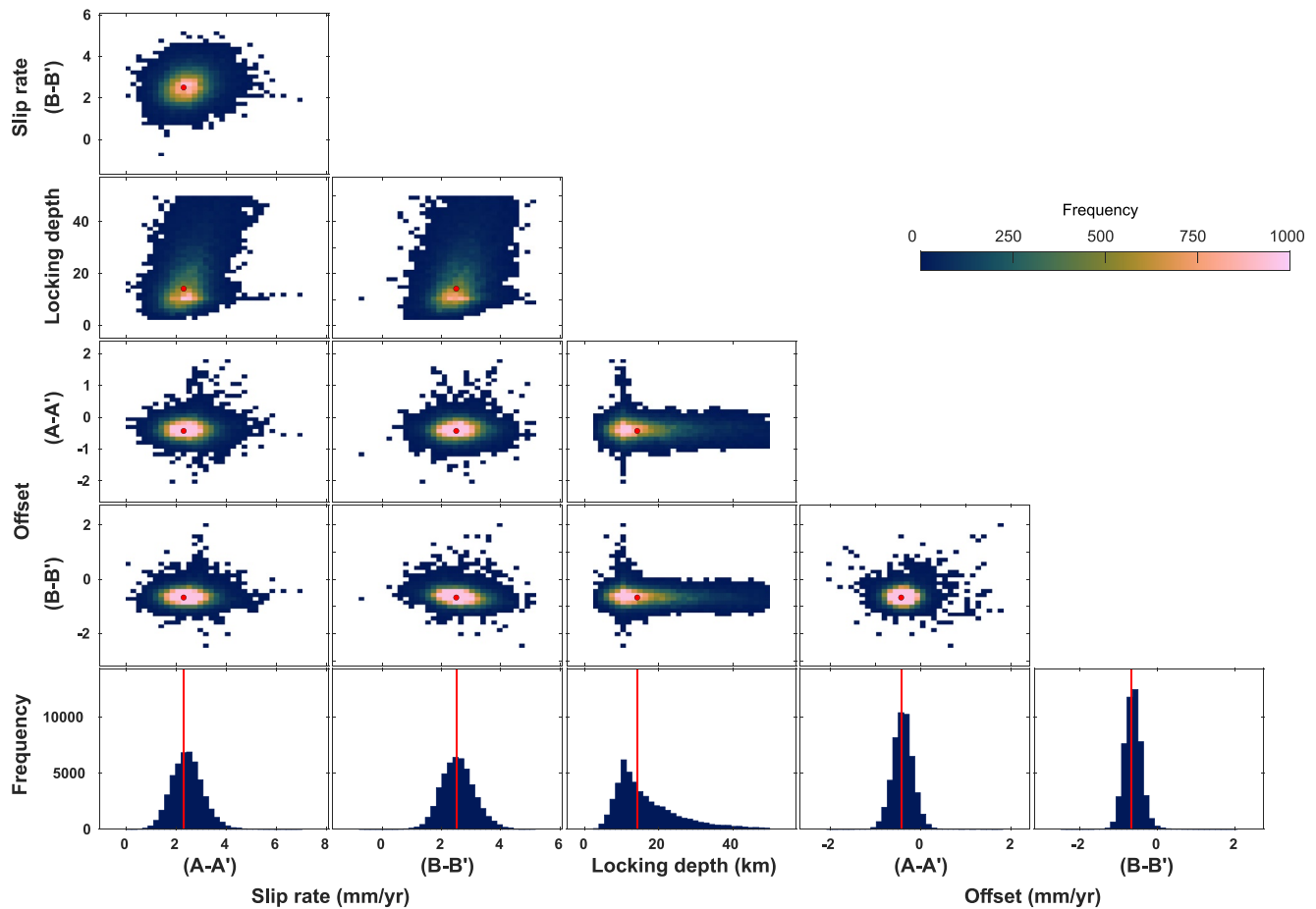


Figure 11. Marginal probability distribution for the profiles in Figure 10, including the MAP solution (red line and dot), for the MCMC inversion (48,000 solutions) under the assumption of a single locking depth along strike of the MRF (i.e., a common joint locking depth for all both profiles). We assume a uniform prior for all model parameters based upon limits on the values of slip rate (−10 to 20 mm/yr), locking depth (1–50 km), and offset (−10 to 10 mm/yr).

The improved upper bound on our joint estimate of the locking depth may be a result of the averaging of the long wavelength trend either side of the fault, which eliminates some unrealistically deep values. Our posterior distribution for the joint locking depth estimate is in line with typical locking depth uncertainties from InSAR (e.g., Karimzadeh et al., 2013; Walters et al., 2011), although narrower uncertainties are achievable with higher slip rates (e.g., Fattahi & Amelung, 2016; H. Wang et al., 2009). Calibrated earthquake locations for the MRF from Karasözen et al. (2019) show a maximum centroid depth of roughly 15–20 km, suggesting that the fault is locked to around this depth. Examining the fault-parallel projected GNSS velocities from Khorrami et al. (2019) shown in Figures 8 and 10, we can see that the local GNSS network lacks suitable station density around the fault trace to capture the velocity gradient, and thus estimate the locking depth.

The wavelength of the velocity gradient across the fault trace is primarily controlled by the locking depth (Equation 6). Most of the strain is accommodated within a distance either side of the fault that is similar to a few times the locking depth. Figure 12 shows the weighted least squares estimates of slip rate for fixed values of locking depth between 1 and 50 km, along with the normalised RMS misfit between the model (Equation 6) and the fault-parallel velocities, for each individual profile and with a joint locking depth as in Figure 11. We weight the least squares with the same variance-covariance matrix as used for the Bayesian analysis. For all three profiles and the joint model, we observe a strong trade-off between the interseismic slip rate on the fault and the locking depth, from 1 to 2 mm/yr at 1 km to 3.0–3.5 mm/yr at 50 km. The magnitude of this trade-off is greatest for locking depths below 10 km. The normalised RMS misfit shows a narrow minimum for profile A-A' (4–10 km) and larger minimums for profile B-B' (8–17 km) and the joint model (7–15 km). The misfit for C-C' shows a local minimum at 5 km and a potential global minimum beyond 50 km, in agreement with the unbounded distribution

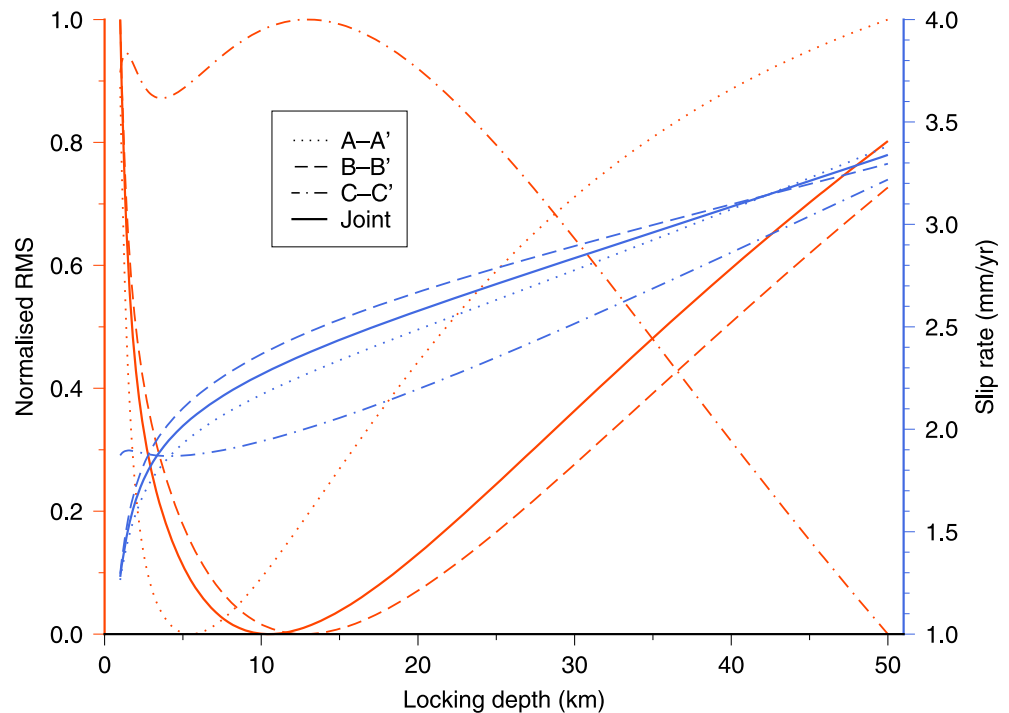


Figure 12. Trade-off between the weighted least-squares estimate of slip rate (blue lines) and fixed values of locking depth for profiles A-A' (dotted line), B-B' (dashed line), C-C' (dot-dashed line), and the joint profiles (solid line). In the case of the joint profiles, where we solve for two slip rates and two offsets, the average slip for both profiles is shown. The normalised root mean square (RMS) misfit (red lines) between the forward model and the observations highlights a minimum for both B-B' and the joint profiles between 10 and 15 km, while A-A' gives a lower and narrowed minimum, and C-C' does not reach a minimum.

show in Figure 11. The shallower gradients of the normalised RMS curves demonstrate a low sensitivity of the model fit to deeper locking depths, in agreement with the posterior distributions for the locking depth estimates (Figures 9 and 11).

5.2. Previous Estimates of the Interseismic Slip Rate

We produce MAP estimates of the interseismic slip rate for each profile, along with a second estimate for profiles A-A' and B-B' based upon a shared locking depth. With the exception of profile C-C', for which the estimated slip rate is lowered by the unconstrained locking depth, the slip rate estimates are grouped between 2.3 and 2.5 mm/yr. In both cases, the minimum of the confidence interval is above 0 mm/yr, and so we can be reasonably confident that the fault is actively accumulating strain in a right-lateral sense. We calculate a mean slip rate of 2.2 ± 1.4 mm/yr (2σ) for all three individual profile estimates, and 2.4 ± 1.2 mm/yr (2σ) for just profiles A-A' and B-B'. We do not calculate a mean and uncertainty from the joint slip rates, as the shared locking depth means that these estimates are not independent. However, the range of estimates (2.3–2.5 mm/yr) is in agreement with the average individual rates. We continue our discussion using the slip rate of 2.4 ± 1.2 mm/yr (2σ) as this is not biased by the unconstrained locking depth in profile C-C'.

These slip rate estimates are comparable to some of the slowest InSAR-derived interseismic slip rates in the literature. Bell et al. (2011) estimated a rate of 3 ± 2 mm/yr for the Manyi fault, Tibet, using 10 ERS images over 5 years to form long-period interferograms. Mousavi et al. (2015) estimated a similar rate of 4.75 ± 0.8 mm/yr for the Shahroud fault, northeast Iran, from 45 Envisat images over a 7 year period. Both studies highlight the importance of the length of the time series over the number of images when resolving slow slip rates. The low slip rate estimate for the Manyi fault was possible partly due to the lack of significant atmospheric noise, both because of low topographic variation along the profile, and because of the arid climate of the high Tibetan Plateau. The latter also allowed for long temporal baseline interferograms with sufficient coherence to obtain reasonable

coverage of the tectonic signal, although we note that the velocity field is patchy. Bell et al. (2011) also highlight the difficulty in constraining the locking depth for signals of this magnitude, with their Monte Carlo solutions reaching their limits of 0–40 km. Mousavi et al. (2015) provides a narrower locking depth estimate of 10 ± 4 km (66% CI), although the result is still relatively insensitive to the choice of locking depth in comparison to the choice of slip rate.

Our range of slip rate estimates is in agreement with previous GNSS-derived estimates for the Main Recent Fault from Vernant et al. (2004) (3 ± 2 mm/yr) and Khorrami et al. (2019) (2.7–4 mm/yr), along with the geological/geomorphological-derived estimates from Alipoor et al. (2012) (1.6–3.2 mm/yr) and Copley and Jackson (2006) (2–5 mm/yr). Our estimates are lower than other geological/geomorphological-derived estimates from Talebian and Jackson (2002) (10–17 mm/yr) and Bachmanov et al. (2004) (10 mm/yr), lower than the GNSS-derived estimate from Walpersdorf et al. (2006) (4–6 mm/yr), and comparable to the lower end of estimates from Authemayou et al. (2009) (3.5–12.5 mm/yr). Whilst our InSAR results are not entirely independent of the GNSS data, as the GNSS data from Khorrami et al. (2019) are used to unify the references of the InSAR velocities, the InSAR data does provide an additional constraint. If we include the North GNSS velocities in our calculation of the fault-parallel velocities, our MAP estimates of slip rate for profiles A-A', B-B', and C-C' increase (2.7, 2.8, and 3.5 mm/yr) along with the locking depths (20.0, 19.1, and 49.8 km; Figures S17 and S18 in Supporting Information S1). The increased locking depths may result from our interpolation of the GNSS velocities, which smooths the gradient of the velocities across the fault trace, increasing the estimated locking depth and in turn increasing the estimated slip rates. The higher slip rates may also suggest that our InSAR-only estimate of fault-parallel velocity is an underestimate, which is in agreement with our slip rate results tending toward the lower end of previous GNSS-derived rates.

Our InSAR-derived velocity fields and fault modeling suggest that the component of motion parallel to the tectonic boundary between the Arabian plate and Iran in our study area is localized onto the MRF. We expand on this by calculating the percentage of partitioned strike-slip motion accommodated by the MRF across the northwestern Zagros. We take a subset of GNSS velocities from Khorrami et al. (2019), located either side of the northwestern Zagros (Figure S11 in Supporting Information S1), and calculate the difference between the weighted mean velocities. We assume a single range-strike of 310° and decompose the velocity difference into range-parallel and range-perpendicular components with values of 4.3 mm/yr and 5.3 mm/yr, respectively. Our interseismic slip rate estimate of 2.4 ± 1.2 mm/yr for the MRF would account for 28%–84% of the overall strike-slip component. At the upper end, this suggests that movement along the MRF alone is sufficient to account for the strike-slip component across this part of the Zagros. At the lower end, this would suggest that strike-slip motion also occurs on adjacent faults, either outside of our study area or with slip rates below our sensing limit, or that a component of the range-parallel motion is accommodated by off-fault deformation. A component of the range-parallel motion will be associated with the overall plate rotation, and so the percentage of range-parallel motion accommodated by the MRF is likely toward the higher end of the proposed range. This is in agreement with block modeling from Khorrami et al. (2019), who estimate 2.7–4 mm/yr of fault-parallel motion along the MRF, and a smaller 0.5 mm/yr fault-parallel component in the Frontal fault zone, which shares a similar strike to the MRF between 46°E and 50°E . The localisation of strike-slip motion paired with distributed thrust faulting has also been observed in the Qilian Shan, northeastern Tibetan Plateau (Allen et al., 2017). Allen et al. (2017) suggest that this arrangement, previously observed in oblique oceanic subduction zones (McCaffrey et al., 2000), may apply generally to oblique convergence zones. Slip is likely to have localized on the MRF because it follows the suture between the Arabian margin and the Iranian block, a pre-existing zone of weakness (Berberian, 1995; Dashti et al., 2020; Walpersdorf et al., 2006).

The localisation of slip on the MRF poses a greater risk of higher magnitude earthquakes than if the deformation was distributed on smaller faults. Given the simplistic scenario that all accumulated strain on the MRF is released seismically by only M_w 7 earthquakes, we can calculate an average recurrence interval for a M_w 7 earthquake similar to the 1909 Dorud earthquake (Ambraseys & Moynfar, 1973) occurring on the fault (e.g., Walters et al., 2014). Assuming an interseismic slip rate of 1–3 mm/yr, on a vertical strike slip fault with a locking depth of 14 km (from our joint model), a shear modulus of 3×10^{10} Pa and a slip-to-length ratio of 3×10^{-5} , we estimate a recurrence time of 530–1590 years.

In our modeling, we do not see any clear signals from interseismic slip at depth on adjacent faults. However, we must be open to the possibility of known or unmapped faults whose signals may be within the noise of

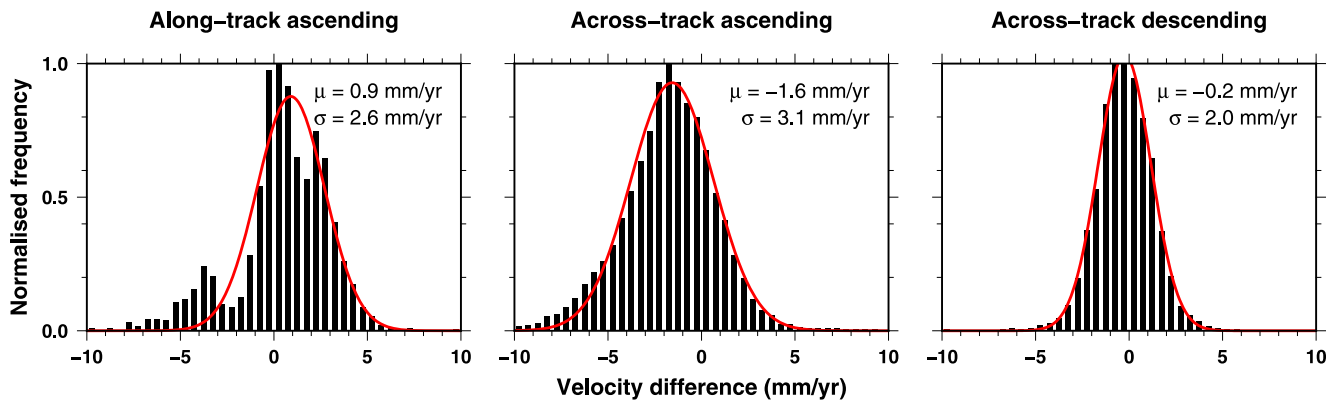


Figure 13. Histograms for the difference between projected horizontal velocities in frame overlaps along ascending tracks (174A-N and 174A-S), across ascending tracks (174A-N, 174A-S, and 101A), and across descending tracks (006D and 108D). Best fitting Gaussians are shown in red, along with their mean, μ , and standard deviation, σ .

our velocities. To the north of the MRF, there are no mapped faults within the collection provided by Walker et al. (2010) within 100 km (Figure 1b). To the south, the nearest fault is 30–40 km away over the area that we profile. Examining the Vertical and East velocities, we see no clear change in velocities across this fault (Figure S14 in Supporting Information S1). Slip on an adjacent fault could increase both the estimated slip rate for the MRF, along with increasing the estimated locking depth by interfering with the velocity gradient across the MRF.

Our estimates for both the interseismic slip rate and the locking depth of the MRF must be kept in the context of our modeling limitations. The poor signal-to-noise ratio of our tectonic signal limited the number of model parameters we were able to constrain. Our screw dislocation model (Equation 6) assumes that all interseismic slip can be reasonably approximated as being localized onto a single vertical plane. Source modeling of the 2006 M_w 6.1 Silakhour earthquake (Ghods et al., 2012; Peyret et al., 2008), which ruptured two segments of the MRF, suggests that the dip of the MRF may be as low as 60°, in agreement with teleseismic crustal imaging (Dashti et al., 2020), with the effect of shifting the shear zone up to 10 km north of the fault trace. This would artificially increase our estimated locking depth by worsening the fit of our model to the velocity gradient across the fault. We would expect the estimated slip rate to be largely unaffected as this is dependent upon the total velocity step across the fault. We also assume identical rheological parameters either side of the MRF, which in reality forms the boundary between the High Zagros and the Central Iranian Plateau (Allen et al., 2013). A contrast in rheological properties across the fault can produce an asymmetric signal, which may in turn result in an overestimated slip rate when using a symmetrical screw dislocation model. Future work may incorporate longer InSAR time series, including images for other InSAR satellites such as Envisat and ERS, to improve the signal-to-noise ratio and to attempt to model a more complex fault geometry and rheological contrasts (e.g., Jolivet et al., 2008)

5.3. Modeling Velocity Uncertainties

Given our low interseismic slip rate estimate for the MRF, one of the slowest InSAR-derived fault slips rates published so far, it is valuable to assess the uncertainties associated with our InSAR velocities. Bootstrapped estimates of the InSAR velocity uncertainty have been shown to decrease with increasing time series length (Morishita et al., 2020), with a 2 mm/yr standard deviation achievable with 1.4 and 1.8 years of 6 and 12 days acquisitions, respectively. Uncertainties for combined GNSS and InSAR velocities, however, may level off around 2–3 mm/yr as the uncertainty on the GNSS velocities becomes dominant (Weiss et al., 2020). As another estimate of the uncertainties, and to examine the effectiveness of the InSAR referencing, we calculate the difference in velocities (Figure 13) between overlapping frames (Walters et al., 2014). We assume that all velocities are purely horizontal by dividing by the sine of the incidence angle and then multiplying by the incidence angle at the center of each frame. The frame overlap between 174A-N and 174A-S covers part of the Sarpol earthquake cluster, meaning our assumption of only horizontal velocities is poor. Despite this, we still observe 1σ uncertainties of less than 3.1 mm/yr, inline with those observed in previous studies (Hussain, Hooper, et al., 2016; Liu et al., 2018; Weiss et al., 2020). This implies that the referencing of the InSAR LOS velocities to a Eurasia-fixed frame has been reasonably successful. These standard deviations can be considered as $\sqrt{2}\times$ the velocity uncertainty for each frame.

This gives a 1σ uncertainty of 1.41 mm/yr for 006D and 108D. For the ascending frames we take the mean of the along-track and across-track values, giving a 1σ uncertainty of 2.02 mm/yr for 174 and 101A.

Our estimated LOS velocities may be biased by fading signals (Ansari et al., 2020), a systemic bias that can accumulate from short-temporal baseline multilooked interferograms. Our small-baseline networks, which primarily consist of connections between each image and three temporally-adjacent images (Figure S1 in Supporting Information S1), are potentially susceptible to this bias. The fading signal is thought to result from changes in soil moisture and biomass (De Zan & Gomba, 2018; De Zan et al., 2015). The largely arid nature of our study area (see NDVI in Figure S15 in Supporting Information S1) should mean that these effects are relatively minimal. Where NDVI is high, we often observe large subsidence signals associated with groundwater extraction. The magnitude of these signals (tens of millimeters per year) are likely significantly larger than any fading bias, and we mask areas in the East velocities associated with large vertical signals (± 10 mm/yr). Despite these factors, the potential of fading bias to have impacted our InSAR velocities must be considered when evaluating our results. Future studies could generate networks with a larger proportion of long temporal-baseline interferograms, or attempt to mitigate any fading bias with empirical corrections.

The final source of uncertainty we address is our method of transforming our relative InSAR velocities into a Eurasia-fixed reference frame using published GNSS horizontal velocities. This method was developed from the works of Hussain, Hooper, et al. (2016), Hussain et al. (2018), Weiss et al. (2020), who applied the method to InSAR velocities over Turkey. While the referencing performed well, with small differences between overlapping tracks, this was based on the reasonable assumption of Anatolia behaving as a rigid block, with deformation concentrated on a couple key fault structures (the North and East Anatolian Faults) and with no known long-wavelength vertical deformation signals. In contrast, the Zagros is a band of diffuse deformation with motion on buried thrust faults (Berberian, 1995; Hatzfeld et al., 2010; Karasözen et al., 2019; Khorrami et al., 2019). If our interpolated GNSS velocities are missing long-wavelength motion that is present in the InSAR velocities, then our referencing polynomial will over or underestimate the true transformation into a Eurasia-fixed reference frame. This, in turn, may bias our estimated model parameter values of slip rate and locking depth. Figures S19 and S20 show the difference between the frame overlaps and estimated models parameters for profile B-B' for velocities referenced with a first order polynomial surface versus a second order polynomial surface. We observe smaller frame overlap differences for a second order polynomial, supporting our choice in the main study, and minimal differences in the estimated locking depth between the two methods. This latter point suggests that the choice of referencing polynomial is having only a small difference on the velocity gradient across the fault. The larger 0.5 mm/yr difference in the estimated slip rate still suggests some sensitivity to the referencing polynomial used, but this change is within the posterior uncertainties. Future works could seek to better constrain long-wavelength motions, including in the vertical direction, although this would be reliant on the deployment of new GNSS stations. The abundance of non-tectonics signals across Iran, such as the groundwater subsidence signals observed in our own InSAR velocities, could also make it difficult to isolate long-wavelength vertical deformation. Instead, methods to derive absolute motion from InSAR observations (e.g., Xu & Sandwell, 2019) may prove more fruitful in referencing velocities.

6. Conclusion

We have used over 5.5 years of Sentinel-1 SAR images across two ascending and two descending tracks to produce the first InSAR-derived estimate of interseismic slip rate for the Main Recent Fault, SW Iran. We combine InSAR LOS velocities with GNSS to estimate the fault-parallel velocity for three across-fault profiles which we model both individually and together to better constrain the fault parameters. Our estimated rate of 2.4 ± 1.2 mm/yr for the MRF between 47°E and 50°E is in agreement with previous geodetic rates from GNSS studies, and is one of the slowest interseismic slip rates measured using InSAR. We provide the first estimate of the locking depth of the fault (14 km), associated with a large uncertainty of 6–40 km, and highlight the difficulties of modeling tectonic signals close to the current InSAR noise level. Our results demonstrate that the MRF is an important major crustal structure that shows a localisation of strain at depth, and that it is possible to measure small tectonic signals on sub-optimal faults in the presence of significant noise.

Data Availability Statement

The Sentinel-1 InSAR data are copyrighted by the European Space Agency and provided freely through the Copernicus Open Access Hub (<https://scihub.copernicus.eu/>). Sentinel-1 InSAR data are also freely distributed by the Alaska Satellite Facility (<https://asf.alaska.edu/>). Processed SAR images, wrapped interferograms, and unwrapped interferograms used in this work can be found on the COMET-LiCS Sentinel-1 InSAR portal (<https://comet.nerc.ac.uk/COMET-LiCS-portal/>). Information on accessing the LiCSBAS software can be found in Morishita et al. (2020). Information on accessing the GACOS atmospheric corrections can be found in Yu, Li, Penna, and Crippa (2018).

Acknowledgments

We thank Milan Lazecky and Yasser Maghsoudi Mehrani for assistance with the LiCSAR processing tools, and Yu Morishita for assistance with the LiCSBAS software. Figures were made using the Generic Mapping Tools (GMT, Wessel et al., 2013). Our thanks also to the Editor, Associate Editor, and both reviewers at JGR: Solid Earth, for a wealth of feedback which significantly improved this work. Andrew Watson is supported through a PhD studentship from the Royal Society (RG/R1180076). This work is supported by the UK Natural Environment Research Council (NERC) through the Centre for the Observation and Modelling of Earthquakes, Volcanoes and Tectonics (COMET, <http://comet.nerc.ac.uk>). This work is also supported by NERC through the Looking into the Continents from Space (LiCS) large Grant (NE/K010867/1). John Elliott acknowledges support from the Royal Society through a University Research Fellowship (UF150282).

References

- Aghajany, S. H., Voosoghi, B., & Yazdian, A. (2017). Estimation of north Tabriz Fault parameters using neural networks and 3D tropospherically corrected surface displacement field. *Geomatics, Natural Hazards and Risk*, 8(2), 918–932.
- Alipoor, R., Zaré, M., & Ghassemi, M. R. (2012). Inception of activity and slip rate on the Main Recent Fault of Zagros Mountains, Iran. *Geomorphology*, 175, 86–97.
- Allen, M., Jackson, J., & Walker, R. (2004). Late Cenozoic reorganization of the Arabia-Eurasia collision and the comparison of short-term and long-term deformation rates. *Tectonics*, 23(2).
- Allen, M., Saville, C., Blanc, E.-P., Talebian, M., & Nissen, E. (2013). Orogenic plateau growth: Expansion of the Turkish-Iranian Plateau across the Zagros fold-and-thrust belt. *Tectonics*, 32(2), 171–190.
- Allen, M., Walters, R. J., Song, S., Saville, C., De Paola, N., Ford, J., et al. (2017). Partitioning of oblique convergence coupled to the fault locking behavior of fold-and-thrust belts: Evidence from the Qilian Shan, Northeastern Tibetan Plateau. *Tectonics*, 36(9), 1679–1698.
- Ambraseys, N., & Moynar, A. (1973). The seismicity of Iran, the Silakhor (Lurestan) earthquake of 23rd. January 1909. *Annals of Geophysics*, 26(4), 659–678.
- Ansari, H., De Zan, F., & Parizzi, A. (2020). Study of systematic bias in measuring surface deformation with sar interferometry. *IEEE Transactions on Geoscience and Remote Sensing*, 59(2), 1285–1301.
- Aslan, G., Lasserre, C., Cakir, Z., Ergintav, S., Özarpci, S., Dogan, U., et al. (2019). Shallow creep along the 1999 Izmit Earthquake rupture (Turkey) from GPS and high temporal resolution interferometric synthetic aperture radar data (2011–2017). *Journal of Geophysical Research: Solid Earth*, 124(2), 2218–2236.
- Authemayou, C., Bellier, O., Chardon, D., Benedetti, L., Malekzade, Z., Claude, C., et al. (2009). Quaternary slip-rates of the Kazerun and the Main Recent Faults: Active strike-slip partitioning in the Zagros fold-and-thrust belt. *Geophysical Journal International*, 178(1), 524–540.
- Bachmanov, D., Trifonov, V., Hessami, K. T., Kozhurin, A., Ivanova, T., Rogozhin, E., et al. (2004). Active faults in the Zagros and central Iran. *Tectonophysics*, 380(3–4), 221–241.
- Barnhart, W. D., Brengman, C. M., Li, S., & Peterson, K. E. (2018). Ramp-flat basement structures of the Zagros Mountains inferred from co-seismic slip and afterslip of the 2017 Mw 7.3 Darbandikhan, Iran/Iraq earthquake. *Earth and Planetary Science Letters*, 496, 96–107.
- Bell, M., Elliott, J., & Parsons, B. (2011). Interseismic strain accumulation across the Manyi fault (Tibet) prior to the 1997 Mw 7.6 earthquake. *Geophysical Research Letters*, 38(24).
- Berberian, M. (1995). Master “blind” thrust faults hidden under the Zagros folds: Active basement tectonics and surface morphotectonics. *Tectonophysics*, 241(3–4), 193–224.
- Biggs, J., Wright, T., Lu, Z., & Parsons, B. (2007). Multi-interferogram method for measuring interseismic deformation: Denali Fault, Alaska. *Geophysical Journal International*, 170(3), 1165–1179.
- Biggs, J., & Wright, T. J. (2020). How satellite InSAR has grown from opportunistic science to routine monitoring over the last decade. *Nature Communications*, 11(1), 1–4.
- Bird, P. (2003). An updated digital model of plate boundaries. *Geochemistry, Geophysics, Geosystems*, 4(3).
- Chen, C. W., & Zebker, H. A. (2000). Network approaches to two-dimensional phase unwrapping: Intractability and two new algorithms. *Journal of the Optical Society of America A*, 17(3), 401–414.
- Chen, C. W., & Zebker, H. A. (2001). Two-dimensional phase unwrapping with use of statistical models for cost functions in nonlinear optimization. *Journal of the Optical Society of America A*, 18(2), 338–351.
- Chen, C. W., & Zebker, H. A. (2002). Phase unwrapping for large SAR interferograms: Statistical segmentation and generalized network models. *IEEE Transactions on Geoscience and Remote Sensing*, 40(8), 1709–1719.
- Copley, A., & Jackson, J. (2006). Active tectonics of the Turkish-Iranian plateau. *Tectonics*, 25(6).
- Dashti, F., Lucente, F. P., Motaghi, K., Bianchi, I., Najafi, M., Govoni, A., & Shabanian, E. (2020). Crustal scale imaging of the Arabia-Central Iran collision boundary across the Zagros suture zone, west of Iran. *Geophysical Research Letters*, 47(8), e2019GL085921.
- De Zan, F., & Gomba, G. (2018). Vegetation and soil moisture inversion from sar closure phases: First experiments and results. *Remote Sensing of Environment*, 217, 562–572.
- De Zan, F., Zonno, M., & Lopez-Dekker, P. (2015). Phase inconsistencies and multiple scattering in sar interferometry. *IEEE Transactions on Geoscience and Remote Sensing*, 53(12), 6608–6616.
- Doin, M.-P., Guillaso, S., Jolivet, R., Lasserre, C., Lodge, F., Ducret, G., & Grandin, R. (2011). Presentation of the small baseline NSBAS processing chain on a case example: The Etna deformation monitoring from 2003 to 2010 using Envisat data. In *Proceedings of the fringe symposium* (pp. 3434–3437).
- Efron, B., & Tibshirani, R. (1986). Bootstrap methods for standard errors, confidence intervals, and other measures of statistical accuracy. *Statistical Science*, 54–75.
- Farr, T. G., Rosen, P. A., Caro, E., Crippen, R., Duren, R., Hensley, S., et al. (2007). The shuttle radar topography mission. *Reviews of Geophysics*, 45(2).
- Fattahi, H., & Amelung, F. (2016). InSAR observations of strain accumulation and fault creep along the Chaman Fault system, Pakistan and Afghanistan. *Geophysical Research Letters*, 43(16), 8399–8406.
- Fialko, Y. (2006). Interseismic strain accumulation and the earthquake potential on the southern San Andreas fault system. *Nature*, 441(7096), 968–971.

- Ghods, A., Rezapour, M., Bergman, E., Mortezaejad, G., & Talebian, M. (2012). Relocation of the 2006 Mw 6.1 Silakhour, Iran, earthquake sequence: Details of fault segmentation on the Main Recent Fault. *Bulletin of the Seismological Society of America*, *102*(1), 398–416.
- Goodman, J., & Weare, J. (2010). Ensemble samplers with affine invariance. *Communications in Applied Mathematics and Computational Science*, *5*(1), 65–80.
- Goto, H., Toyomasu, A., & Sawada, S. (2019). Delayed subevents during the Mw 6.2 first shock of the 2016 Kumamoto, Japan, earthquake. *Journal of Geophysical Research: Solid Earth*, *124*(12), 13112–13123.
- Hatzfeld, D., Authemayou, C., van der Beek, P., Bellier, O., Lavé, J., Oveisi, B., et al. (2010). The kinematics of the Zagros Mountains (Iran). *Geological Society, London, Special Publications*, *330*(1), 19–42.
- Hatzfeld, D., & Molnar, P. (2010). Comparisons of the kinematics and deep structures of the Zagros and Himalaya and of the Iranian and Tibetan plateaus and geodynamic implications. *Reviews of Geophysics*, *48*(2).
- Hessami, K., Nilforoushan, F., & Talbot, C. J. (2006). Active deformation within the Zagros Mountains deduced from GPS measurements. *Journal of the Geological Society*, *163*(1), 143–148.
- Hussain, E., Hooper, A., Wright, T. J., Walters, R. J., & Bekaert, D. P. (2016). Interseismic strain accumulation across the central North Anatolian Fault from iteratively unwrapped InSAR measurements. *Journal of Geophysical Research: Solid Earth*, *121*(12), 9000–9019.
- Hussain, E., Wright, T. J., Walters, R. J., Bekaert, D., Hooper, A., & Houseman, G. A. (2016). Geodetic observations of postseismic creep in the decade after the 1999 Izmit earthquake, Turkey: Implications for a shallow slip deficit. *Journal of Geophysical Research: Solid Earth*, *121*(4), 2980–3001.
- Hussain, E., Wright, T. J., Walters, R. J., Bekaert, D. P., Lloyd, R., & Hooper, A. (2018). Constant strain accumulation rate between major earthquakes on the North Anatolian Fault. *Nature Communications*, *9*(1), 1–9.
- Jolivet, R., Cattin, R., Chamot-Rooke, N., Lasserre, C., & Peltzer, G. (2008). Thin-plate modeling of interseismic deformation and asymmetry across the Altn Tagh fault zone. *Geophysical Research Letters*, *35*(2).
- Jolivet, R., Lasserre, C., Doin, M.-P., Peltzer, G., Avouac, J.-P., Sun, J., & Dailu, R. (2013). Spatio-temporal evolution of aseismic slip along the Haiyuan Fault, China: Implications for fault frictional properties. *Earth and Planetary Science Letters*, *377*, 23–33.
- Karasözen, E., Nissen, E., Bergman, E. A., & Ghods, A. (2019). Seismotectonics of the Zagros (Iran) from orogen-wide, calibrated earthquake relocations. *Journal of Geophysical Research: Solid Earth*, *124*(8), 9109–9129.
- Karimzadeh, S., Cakir, Z., Osmanoğlu, B., Schmalzle, G., Miyajima, M., Amiraslazadeh, R., & Djamour, Y. (2013). Interseismic strain accumulation across the North Tabriz Fault (NW Iran) deduced from InSAR time series. *Journal of Geodynamics*, *66*, 53–58.
- Khorrami, F., Vernant, P., Masson, F., Nilfouroushan, F., Mousavi, Z., Nankali, H., et al. (2019). An up-to-date crustal deformation map of Iran using integrated campaign-mode and permanent GPS velocities. *Geophysical Journal International*.
- Kreemer, C., Blewitt, G., & Klein, E. C. (2014). A geodetic plate motion and global strain rate model. *Geochemistry, Geophysics, Geosystems*, *15*(10), 3849–3889.
- Lazecký, M., Spaans, K., González, P. J., Maghsoudi, Y., Morishita, Y., Albino, F., et al. (2020). LiCSAR: An automatic InSAR tool for measuring and monitoring tectonic and volcanic activity. *Remote Sensing*, *12*(15), 2430.
- Liu, C., Ji, L., Zhu, L., & Zhao, C. (2018). InSAR-constrained interseismic deformation and potential seismogenic asperities on the Altn Tagh fault at 91.5–95 E, Northern Tibetan Plateau. *Remote Sensing*, *10*(6), 943.
- Lv, X., Amelung, F., Shao, Y., Ye, S., Liu, M., & Xie, C. (2020). Rheology of the zagros lithosphere from post-seismic deformation of the 2017 Mw 7.3 Kermanshah, Iraq, earthquake. *Remote Sensing*, *12*(12), 2032.
- Masson, F., Chéry, J., Hatzfeld, D., Martinod, J., Vernant, P., Tavakoli, F., & Ghafoory-Ashtiani, M. (2005). Seismic versus aseismic deformation in Iran inferred from earthquakes and geodetic data. *Geophysical Journal International*, *160*(1), 217–226.
- McCaffrey, R., Zwick, P. C., Bock, Y., Prawirodirdjo, L., Genrich, J. F., Stevens, C. W., et al. (2000). Strain partitioning during oblique plate convergence in northern Sumatra: Geodetic and seismologic constraints and numerical modeling. *Journal of Geophysical Research: Solid Earth*, *105*(B12), 28363–28376.
- McClusky, S., Reilinger, R., Mahmoud, S., Ben Sari, D., & Tealeb, A. (2003). GPS constraints on Africa (Nubia) and Arabia plate motions. *Geophysical Journal International*, *155*(1), 126–138.
- Morishita, Y. (2021). Nationwide urban ground deformation monitoring in Japan using Sentinel-1 LiCSAR products and LiCSBAS. *Progress in Earth and Planetary Science*, *8*(1), 1–23.
- Morishita, Y., Lazecky, M., Wright, T. J., Weiss, J. R., Elliott, J. R., & Hooper, A. (2020). LiCSBAS: An open-source InSAR time series analysis package integrated with the LiCSAR automated Sentinel-1 InSAR processor. *Remote Sensing*, *12*(3), 424.
- Mousavi, Z., Fattahi, M., Khatib, M., Talebian, M., Pathier, E., Walpersdorf, A., et al. (2021). Constant slip-rate on the Doruneh strike-slip fault, Iran, averaged over Late Pleistocene, Holocene, and decadal timescales. *Tectonics*, e2020TC006256.
- Mousavi, Z., Pathier, E., Walker, R., Walpersdorf, A., Tavakoli, F., Nankali, H., et al. (2015). Interseismic deformation of the Shahroud fault system (NE Iran) from space-borne radar interferometry measurements. *Geophysical Research Letters*, *42*(14), 5753–5761.
- Niassarifard, M., Shabaniyan, E., Azad, S. S., & Madanipour, S. (2021). New tectonic configuration in NW Iran: Intracontinental dextral shear between NW Iran and SE Anatolia. *Tectonophysics*, 228886.
- Nippress, S. E., Heyburn, R., & Walters, R. (2017). The 2008 and 2012 Moosiyen earthquake sequences: Rare insights into the role of strike slip and thrust faulting within the simply folded belt (Iran). *Bulletin of the Seismological Society of America*, *107*(4), 1625–1641.
- Nissen, E., Ghods, A., Karasözen, E., Elliott, J. R., Barnhart, W. D., Bergman, E. A., et al. (2019). The 12 November 2017 Mw 7.3 Ezgeleh-Sarpolzhah (Iran) earthquake and active tectonics of the Lurestan arc. *Journal of Geophysical Research: Solid Earth*.
- Nissen, E., Tatar, M., Jackson, J. A., & Allen, M. B. (2011). New views on earthquake faulting in the Zagros fold-and-thrust belt of Iran. *Geophysical Journal International*, *186*(3), 928–944.
- Okada, Y. (1985). Surface deformation due to shear and tensile faults in a half-space. *Bulletin of the Seismological Society of America*, *75*(4), 1135–1154.
- Parker, A. L., Biggs, J., Walters, R. J., Ebmeier, S. K., Wright, T. J., Teanby, N. A., & Lu, Z. (2015). Systematic assessment of atmospheric uncertainties for InSAR data at volcanic arcs using large-scale atmospheric models: Application to the Cascade volcanoes, United States. *Remote Sensing of Environment*, *170*, 102–114.
- Peyret, M., Djamour, Y., Hessami, K., Regard, V., Bellier, O., Vernant, P., et al. (2009). Present-day strain distribution across the Minab-Zendan-Palami fault system from dense GPS transects. *Geophysical Journal International*, *179*(2), 751–762.
- Peyret, M., Rolandone, F., Dominguez, S., Djamour, Y., & Meyer, B. (2008). Source model for the Mw 6.1, 31 March 2006, Chalan-Chulan earthquake (Iran) from InSAR. *Terra Nova*, *20*(2), 126–133.
- Rizza, M., Vernant, P., Ritz, J.-F., Peyret, M., Nankali, H., Nazari, H., et al. (2013). Morphotectonic and geodetic evidence for a constant slip-rate over the last 45 kyr along the Tabriz fault (Iran). *Geophysical Journal International*, *193*(3), 1083–1094.

- Savage, J. (2000). Viscoelastic-coupling model for the earthquake cycle driven from below. *Journal of Geophysical Research: Solid Earth*, 105(B11), 25525–25532.
- Savage, J., & Burford, R. (1973). Geodetic determination of relative plate motion in central California. *Journal of Geophysical Research*, 78(5), 832–845.
- Savage, J., & Prescott, W. (1978). Asthenosphere readjustment and the earthquake cycle. *Journal of Geophysical Research: Solid Earth*, 83(B7), 3369–3376.
- Sepahvand, M., Yaminifard, F., Tatar, M., & Abbassi, M. (2012). Aftershocks study of the 2006 Silakhr earthquake (Zagros, Iran): Seismological evidences for a pull-apart basin along the Main Recent Fault, Doroud segments. *Journal of Seismology*, 16(2), 233–251.
- Smith-Konter, B., & Sandwell, D. (2009). Stress evolution of the San Andreas fault system: Recurrence interval versus locking depth. *Geophysical Research Letters*, 36(13).
- Su, Z., Wang, E.-C., Hu, J.-C., Talebian, M., & Karimzadeh, S. (2016). Quantifying the termination mechanism along the North Tabriz-North Mishu fault zone of northwestern Iran via small baseline PS-InSAR and GPS decomposition. *IEEE Journal of Selected Topics in Applied Earth Observations and Remote Sensing*, 10(1), 130–144.
- Szeliga, W., & Bilham, R. (2017). New constraints on the mechanism and rupture area for the 1905 Mw 7.8 Kangra earthquake, northwest Himalaya. *Bulletin of the Seismological Society of America*, 107(5), 2467–2479.
- Talebian, M., & Jackson, J. (2002). Offset on the Main Recent Fault of NW Iran and implications for the late Cenozoic tectonics of the Arabia-Eurasia collision zone. *Geophysical Journal International*, 150(2), 422–439.
- Talebian, M., & Jackson, J. (2004). A reappraisal of earthquake focal mechanisms and active shortening in the Zagros mountains of Iran. *Geophysical Journal International*, 156(3), 506–526.
- Tavakoli, F., Walpersdorf, A., Authemayou, C., Nankali, H., Hatzfeld, D., Tatar, M., et al. (2008). Distribution of the right-lateral strike-slip motion from the Main Recent Fault to the Kazerun Fault system (Zagros, Iran): Evidence from present-day GPS velocities. *Earth and Planetary Science Letters*, 275(3–4), 342–347.
- Tchalenko, J., & Braud, J. (1974). Seismicity and structure of the Zagros (Iran): The Main Recent Fault between 33 and 35 N. *Philosophical Transactions of the Royal Society of London - Series A: Mathematical and Physical Sciences*, 277(1262), 1–25.
- Tesson, J., Benedetti, L., Godard, V., Novaes, C., Fleury, J., & Team, A. (2021). Slip rate determined from cosmogenic nuclides on normal-fault facets. *Geology*, 49(1), 66–70.
- Thatcher, W. (1983). Nonlinear strain build-up and the earthquake cycle on the San Andreas fault. *Journal of Geophysical Research: Solid Earth*, 88(B7), 5893–5902.
- Tong, X., Sandwell, D., & Smith-Konter, B. (2013). High-resolution interseismic velocity data along the San Andreas Fault from GPS and InSAR. *Journal of Geophysical Research: Solid Earth*, 118(1), 369–389.
- Vernant, P., Nilforoushan, F., Hatzfeld, D., Abbassi, M., Vigny, C., Masson, F., et al. (2004). Present-day crustal deformation and plate kinematics in the Middle East constrained by GPS measurements in Iran and northern Oman. *Geophysical Journal International*, 157(1), 381–398.
- Walker, R. T., Talebian, M., Saiffori, S., Sloan, R. A., Rasheedi, A., MacBean, N., & Ghassemi, A. (2010). Active faulting, earthquakes, and restraining bend development near Kerman city in southeastern Iran. *Journal of Structural Geology*, 32(8), 1046–1060.
- Walpersdorf, A., Hatzfeld, D., Nankali, H., Tavakoli, F., Nilforoushan, F., Tatar, M., et al. (2006). Difference in the GPS deformation pattern of North and Central Zagros (Iran). *Geophysical Journal International*, 167(3), 1077–1088.
- Walters, R., Elliott, J., Li, Z., & Parsons, B. (2013). Rapid strain accumulation on the Ashkabad fault (Turkmenistan) from atmosphere-corrected InSAR. *Journal of Geophysical Research: Solid Earth*, 118(7), 3674–3690.
- Walters, R., Holley, R., Parsons, B., & Wright, T. (2011). Interseismic strain accumulation across the north Anatolian fault from Envisat InSAR measurements. *Geophysical Research Letters*, 38(5).
- Walters, R., Parsons, B., & Wright, T. (2014). Constraining crustal velocity fields with InSAR for Eastern Turkey: Limits to the block-like behavior of Eastern Anatolia. *Journal of Geophysical Research: Solid Earth*, 119(6), 5215–5234.
- Wang, H., Wright, T., & Biggs, J. (2009). Interseismic slip rate of the northwestern Xianshuihe fault from InSAR data. *Geophysical Research Letters*, 36(3).
- Wang, K., & Bürgmann, R. (2020). Probing fault frictional properties during afterslip updip and downdip of the 2017 Mw 7.3 Sarpol-e Zahab earthquake with space geodesy. *Journal of Geophysical Research: Solid Earth*, 125(11), e2020JB020319.
- Wegmüller, U., Werner, C., Strozzi, T., Wiesmann, A., Frey, O., & Santoro, M. (2016). Sentinel-1 support in the GAMMA software. *Procedia Computer Science*, 100, 1305–1312.
- Weiss, J. R., Walters, R. J., Morishita, Y., Wright, T. J., Lazecky, M., Wang, H., et al. (2020). High-resolution surface velocities and strain for Anatolia from Sentinel-1 InSAR and GNSS data. *Geophysical Research Letters*, e2020GL087376.
- Werner, C., Wegmüller, U., Strozzi, T., & Wiesmann, A. (2000). Gamma SAR and interferometric processing software. In *Proceedings of the Ers-Envisat Symposium, Gothenburg, Sweden* (Vol. 1620, p. 1620).
- Wessel, P., Smith, W. H., Scharroo, R., Luis, J., & Wobbe, F. (2013). Generic mapping tools: Improved version released. *Eos, Transactions American Geophysical Union*, 94(45), 409–410.
- Wright, T. J., Elliott, J. R., Wang, H., & Ryder, I. (2013). Earthquake cycle deformation and the Moho: Implications for the rheology of continental lithosphere. *Tectonophysics*, 609, 504–523.
- Xu, X., & Sandwell, D. T. (2019). Toward absolute phase change recovery with insar: Correcting for earth tides and phase unwrapping ambiguities. *IEEE Transactions on Geoscience and Remote Sensing*, 58(1), 726–733.
- Yu, C., Li, Z., & Penna, N. T. (2018). Interferometric synthetic aperture radar atmospheric correction using a GPS-based iterative tropospheric decomposition model. *Remote Sensing of Environment*, 204, 109–121.
- Yu, C., Li, Z., Penna, N. T., & Crippa, P. (2018). Generic atmospheric correction model for interferometric synthetic aperture radar observations. *Journal of Geophysical Research: Solid Earth*, 123(10), 9202–9222.
- Yu, C., Penna, N. T., & Li, Z. (2017). Generation of real-time mode high-resolution water vapor fields from GPS observations. *Journal of Geophysical Research: Atmospheres*, 122(3), 2008–2025.
- Zarifi, Z., Nilfouroushan, F., & Raeesi, M. (2014). Crustal stress map of Iran: Insight from seismic and geodetic computations. *Pure and Applied Geophysics*, 171(7), 1219–1236.
- Zebker, H. A., Rosen, P. A., & Hensley, S. (1997). Atmospheric effects in interferometric synthetic aperture radar surface deformation and topographic maps. *Journal of Geophysical Research: Solid Earth*, 102(B4), 7547–7563.